accepted to ApJ
Preprint typeset using LaTeX style emulateapj v. 14/09/00

HIGH-RESOLUTION X-RAY SPECTROSCOPY OF HERCULES X-1 WITH THE *XMM-NEWTON* RGS: CNO ELEMENT ABUNDANCE MEASUREMENTS AND DENSITY DIAGNOSTICS OF A PHOTOIONIZED PLASMA

M. A. Jimenez-Garate,[1,2] C. J. Hailey,[2] J. W. den Herder,[3] S. Zane,[4] and G. Ramsay[4]
accepted to ApJ

ABSTRACT

We analyze the high-resolution X-ray spectrum of Hercules X-1, an intermediate-mass X-ray binary, which was observed with the *XMM-Newton* Reflection Grating Spectrometer. We measure the elemental abundance ratios by use of spectral models, and we detect material processed through the CNO-cycle. The CNO abundances, and in particular the ratio N/O > 4.0 times solar, provide stringent constraints on the evolution of the binary system. The low and short-on flux states of Her X-1 exhibit narrow line emission from C VI, N VI, N VII, O VII, O VIII, Ne IX, and Ne X ions. The spectra show signatures of photoionization. We measure the electron temperature, quantify photoexcitation in the Heα lines, and set limits on the location and density of the gas. The recombination lines may originate in the accretion disk atmosphere and corona, or on the X-ray illuminated face of the mass donor (HZ Her). The spectral variation over the course of the 35 d period provides additional evidence for the precession of the disk. During the main-on state, the narrow line emission is absent, but we detect excesses of emission at $\sim$10–15 Å, and also near the O VII intercombination line wavelength.

Subject headings: X-rays: binaries — line: formation — line: identification — pulsars: individual (Her X-1) — accretion, accretion disks — binaries: eclipsing

1. INTRODUCTION

Hercules X-1 is a bright intermediate-mass X-ray binary which has been observed extensively after its discovery by Schreier et al. (1972). The system contains an X-ray pulsar with $P_{\rm pulse} = 1.24$ s period (Tananbaum et al. 1972; Wilson, Scott, & Finger 1997). A synchrotron resonance feature yields a magnetic field of $B = 3.5 \times 10^{12}$ G (dal Fiume et al. 1998; Truemper et al. 1978). Some models yield a lower magnetic field (Baushev & Bisnovatyi-Kogan 1999). Optical light-curves (Gerend & Boynton 1976) and X-ray eclipses (Tananbaum et al. 1972) yield a $P_{\rm orb} = 1.7$ day orbital period. The $1.5 \pm 0.3\ M_{\odot}$ neutron star has a $2.3 \pm 0.3\ M_{\odot}$ companion, HZ Her, which changes from A to B spectral-type over the orbital period, due to the strong X-ray illumination on its surface (Reynolds et al. 1997). Pre-eclipse and anomalous dips in the X-ray flux are observed (Giacconi et al. 1973; Scott & Leahy 1999) due to the interaction of an accretion stream with the accretion disk. The unabsorbed luminosity of Her X-1 is $L = 3.8 \times 10^{37}$ ergs^{-1}, using a distance of $D = 6.6 \pm 0.4$ kpc (Reynolds et al. 1997).

Hercules X-1 exhibits an unusual long-term X-ray flux modulation with $P_{\Psi} = 35$ d period (Giacconi et al. 1973). Changes associated with this period have also been observed in the optical light curves (Gerend & Boynton 1976), X-ray pulse shapes (Deeter et al. 1991), X-ray dips (Giacconi et al. 1973; Scott & Leahy 1999), and X-ray spectra (Ramsay et al. 2002). The 35 d X-ray light-curve is asymmetric and contains two maxima: a state of ~ 8 d duration reaching the peak flux $F_{\rm max}$ named the *main-on*, and a secondary high state of ~ 4 d duration reaching $\sim 1/3\ F_{\rm max}$ named the *short-on*. A low-flux state with $\sim 1/20\ F_{\rm max}$ ensues at other epochs. The period P_{Ψ} varies from cycle to cycle, and it has been observed to be 19.5, 20, 20.5, and 21 times $P_{\rm orb}$ in the course of $\gtrsim 5$ yr of continuous monitoring with the All-Sky Monitor onboard the *Rossi X-ray Timing Explorer* (Scott & Leahy 1999). The $\Psi = 0$ phase is defined as the time the main-on state begins. Observations indicate that $\Psi = 0$ coincides only with orbital phases $\phi = 0.23$ or 0.68 (Scott & Leahy 1999).

The 35 d cycle has been associated with a tilted accretion disk that precesses by some unknown mechanism (Petterson 1975; Petterson, Rothschild, & Gruber 1991; Scott, Leahy, & Wilson 2000). The X-ray light-curve, the variations in the pulse profiles, and the variability of the dips with Ψ-phase are fit by a geometric model of a precessing, warped accretion disk, together with the beam of a pulsar (Scott, Leahy, & Wilson 2000). Among the parameters obtained in this fit are an 85° inclination with respect to the line of sight, a 20° precession opening angle for the outermost disk, and an 11° precession angle for the innermost disk. The latter precession angles are dependent on assumed input parameters such as the disk thickness.

The ultraviolet (UV) spectrum exhibits line emission from species such as C IV, N V, and O V, which originate in two separate components that produce superimposed broad and narrow lines. The intensity of the narrow lines has the same orbital variation as the UV continuum, which is thought to originate on the illuminated face of HZ Her. The broad line component follows roughly the velocities expected for the accretion disk (Boroson et al.

[1] Center for Space Research, Massachusetts Institute of Technology, 70 Vassar St, NE80-6091, Cambridge, MA, 02139; mario@space.mit.edu.
[2] Columbia Astrophysics Laboratory, New York, NY, 10027; chuckh@astro.columbia.edu.
[3] SRON, the National Institute for Space Research, The Netherlands; J.W.A.den.Herder@sron.nl.
[4] Mullard Space Science Laboratory, University College of London, UK; sz@mssl.ucl.ac.uk, gtbr@mssl.ucl.ac.uk.

1997). Observations during eclipse ingress and egress suggest that the broad line region originates in a prograde disk of $\sim 10^{11}$ cm radius (Boroson et al. 2000). The UV lines (i.e. N V) have a weak P Cygni profile component which indicates the presence of a wind outflow (Chiang 2001).

The Her X-1 broadband X-ray emission can be described as a blackbody component with temperature $kT \sim 90$ eV, plus a power-law component with a 24 keV exponential cutoff, and a 42 keV cyclotron feature (dal Fiume et al. 1998). An Fe K fluorescence line evolves with Ψ-phase. The *XMM-Newton* EPIC data, presented by Ramsay et al. (2002), show a 6.4 keV Fe K line which is practically unresolved during the low and short-on states, and a broad line at 6.5 keV with 330 ± 20 eV FWHM during the main-on.

In this article, we present the high-resolution spectrum of Her X-1 in the 5 to 38 Å band, which we obtained with the *XMM-Newton* Reflection Grating Spectrometer (RGS). The high-resolution X-ray spectrum evolves dramatically with 35 d phase. We analyze the spectral data from three distinct epochs (section 2). The spectrum during the low and short-on states is a faint power-law continuum plus many narrow emission line features from a photoionized plasma (section 3). In contrast, the main-on state has a bright continuum, neutral absorption features, excess of emission near O VII Heα, and a continuum which cannot be fit well with blackbody and/or power-law models (section 4). The observed emission lines arise from the recombination of electrons with ions and from the subsequent radiative cascades. The gas is predominantly heated by photons due to the large luminosity and small volume of the system.

We analyze and model the high-resolution spectra of Her X-1 to obtain the elemental abundance ratios and measure the state variables of the gas, and we make preliminary identifications of the newly detected emission region(s). We apply spectral diagnostics on the plasma to constrain its location (section 3.1), its density (section 3.2), and to measure the electron temperature (section 3.3). We introduce a method to extract the elemental abundance ratios from the low and short-on spectra. The method involves extracting the emission measure distribution from model fits of the recombination line fluxes (section 5). We discuss whether the narrow line emission originates in a disk atmosphere and corona, on the illuminated companion, or in both (section 6.1). We describe the implications of the detection of CNO-processed material for the evolution of the X-ray binary (section 6.2). We outline a physical scenario which produces broad emission lines, which is associated with the magnetopause and the inner disk in X-ray pulsars (section 6.3). In that context, we speculate on the origin of the complex continuum observed during the main-on (section 6.4). Our conclusions are in section 7.

2. OBSERVATIONS

Three observations with *XMM-Newton* RGS during the main-on, short-on and low states, reveal X-ray line emission that varies with Ψ-phase. The *RXTE* All-Sky Monitor (*ASM*) public data are used to find the epoch of main-on start, or $\Psi = 0$ (see the light curve in Fig. 1). The values of the ϕ- and Ψ-phases during the *XMM-Newton* observations are shown in Table 1.

We describe the processing of each RGS spectrum. All the data are processed with the most recent version of the science analysis software (*SAS* v. 5.3). Response matrices are extracted using 4000 energy bins in the full RGS energy range. Hot pixels which are flagged by the pipeline processing are excluded from the analysis. Continuum and line fits are performed with the XSPEC v.11.1 analysis software (Arnaud 1996). The total RGS background count-rate is 0.09 c s^{-1} in the low state, 0.08 c s^{-1} in the short-on state, and ≤ 0.28 c s^{-1} in the main-on state. The background is roughly independent of wavelength, at a level of $\sim 2.7 \times 10^{-3}$ c s^{-1} Å^{-1} in the low and short-on states. The background level rises by a factor of 2 to 4 for wavelengths $\lambda < 7$ Å. The background level in the main-on is very small (≤ 0.015 c s^{-1} Å^{-1}) compared to scattering in the cross-dispersion direction from first order photons. The background-subtracted event lists from the *SAS* pipeline are used throughout. The extraction regions from the RGS data are inspected and left unchanged from the *SAS* default. During main-on, RGS 2 is set to high timing resolution mode, as part of the performance verification of the instrument, while RGS 1 is set to spectroscopy mode. The RGS guaranteed time observations were performed during the low and short-on states, with both RGS in spectroscopy mode. We present the spectroscopy mode data. Since CCD chip 7 in RGS 1 and CCD chip 4 in RGS 2 are not operational, the wavelength ranges of 10.3 to 13.6 Å and 19.9 to 24.9 Å are excluded from each RGS dataset, respectively. For the main-on data, we have enough counts to use the RGS 1 second order, which fills the wavelength gap in the first order.

3. SPECTROSCOPY OF THE LOW AND SHORT-ON STATES

The low-state RGS spectrum (shown in Fig. 2) contains line emission from Ne IX, O VIII, O VII, N VII, N VI and C VI ions. Within the resolution, no velocity broadening has been observed. The continuum shape is described by a power-law, although the goodness-of-fit is likely degraded by a collection of weak and unresolved spectral lines. There is a neutral O edge, which is mostly instrumental. The line and continuum measurements are shown in Tables 2 and 3, respectively. No evidence for absorption local to the source is observed on these states, implying that the line emission region is optically thin to both lines and continuum.

The total RGS count-rate in the short-on is two times larger than during the low-state (also in Fig. 2). There is variability within each observation as well, but we leave that out of our analysis. The line luminosities are usually larger in the short-on than in the low state (Table 2). The better statistics during the short-on allows us to detect the O VII and N VII radiative recombination continua (RRC). On Figure 3, we show the added spectrum of the low and short-on states, which have similar features, to clarify the statistical significance of the detection of Ne IX Heα, C VI Lyα, the O VII RRC, and the N VII RRC (the line profiles in this figure are not adequate for analysis because we have added spectral data with different spectral resolution). The EPIC 0.3–10 keV count rates, which are 398, 54 and 21 c s^{-1} in the main-on, short-on, and low states, respectively (Ramsay et al. 2002), indicate fluxes which are consistent with the long term *XTE ASM* light curve (Scott & Leahy 1999), with our main-on observation near peak, and our short-on observation at half-peak.

Our phenomenological model fit to the spectrum consists of a power-law continuum, emission lines, absorption edges, and RRC. To perform the continuum fits, and to use the χ^2 statistic, we bin the spectrum with a minimum of 20 counts per bin. The spectra shown in Figures 2, 3, and 4 are rebinned as indicated on each caption. The spectral lines are fit at full resolution with Gaussian functions by independently varying their normalization, width, and centroid. The line identifications are shown in Table 2. The continuum is re-fit for accuracy after the line fits are added. The ISIS analysis software (Houck & Denicola 2000) is used to check the line fits from XSPEC. With ISIS, the continuum level is measured in two regions adjacent to the lines. The line equivalent widths (EW) calculated from that continuum level are shown in the last two columns of Table 2. The line fluxes from XSPEC and the equivalent widths measured with ISIS agreed to < 10 %, although the difference is ~ 25 % for N VII Heα, N VI Heα, and O VIII Lyα. The difference is due to some hot pixels which are removed only with XSPEC, and to the uncertainty of the continuum flux level.

3.1. *Helium-like ion emission line diagnostics*

Electron density and temperature measurements in the $10^8 < n_e < 10^{18}$ cm^{-3} and $10^6 < T < 10^7$ K ranges can be obtained with helium-like ion emission line ratios (Gabriel & Jordan 1969; Porquet & Dubau 2000). The dominant ionization mechanism can be determined from the same lines (Liedahl 1999). Low-Mass X-ray binaries (LMXB), and other X-ray binaries with accretion disks, should exhibit densities high enough to render these diagnostics useful.

In Her X-1, the helium-like ion line complexes show a prominent intercombination line blend (i denotes the two transitions $2^3P_{1,2} \rightarrow 1^1S_0$) and a weaker resonance line (r denotes $2^1P_1 \rightarrow 1^1S_0$), as shown in Figures 5 and 6. The forbidden line (f denotes $2^3S_1 \rightarrow 1^1S_0$) is not detected for any of the helium-like ions Ne IX, O VII, and N VI. The notation $n^{2S+1}L_J$ identifies each two-electron atomic state, with quantum numbers n, L, S, and J.

The line ratio $G = (f+i)/r$ is consistent with $\simeq 4$ for all cases shown in Table 4, which indicates that photoionization is the dominant heating mechanism. For collisionally ionized gases, $G \lesssim 1$, decreasing for larger temperatures (Liedahl 1999; Porquet & Dubau 2000). The G ratio indicates the electron temperature is $T < 2 \times 10^6$ K, or $kT < 170$ eV (Porquet & Dubau 2000).

We set upper limits for the $R = f/i$ line ratio (see Tables 2 and 4). The $R \sim 0$ ratio indicates that 1) the density is above the threshold calculated by Porquet & Dubau (2000) and Bautista & Kallman (2000), thereby exciting the 2^3S_1 level to the $2^3P_{1,2}$ levels by electron impact, and/or 2) the 2^3S_1 level is photo-excited to the same $2^3P_{1,2}$ levels, as described by Mewe & Schrijver (1978), and later identified in an O-star wind by Kahn et al. (2001). The density limits implied by the measured R, ignoring photoexcitation, would be $n_e > 4\times10^{11}$ cm^{-3} for N VI, $n_e > 2\times10^{12}$ cm^{-3} for O VII, and $n_e > 5 \times 10^{12}$ cm^{-3} for Ne IX (Porquet & Dubau 2000). However, the photoexcitation rate is

$$w_{\mathrm{f}\rightarrow\mathrm{i}} = \frac{\pi e^2}{m_e c} F_{\nu_{f\rightarrow i}} f_{\mathrm{osc}}, \qquad (1)$$

where e, m_e are the electron charge and mass, c is the speed of light, f_{osc} is the oscillator strength, and $F_{\nu_{f\rightarrow i}}$ is the flux (in photons s^{-1} cm^{-2} Hz^{-1}) at frequencies resonant with the $2^3S_1 \rightarrow 2^3P_{1,2}$ transitions, in this case in the UV. We use the f_{osc} calculated by Cann & Thakkar (1992). The calculated rates (Table 4) imply that UV photoexcitation can compete with electron impact excitation, such that the R ratio density diagnostics are not directly applicable in Her X-1.

Instead, we use the R ratio to set limits on the distance between the X-ray line region and the UV source, d. Because the radiation field is diluted with increasing distance, $w_{\mathrm{f}\rightarrow\mathrm{i}} \propto F_{\nu_{f\rightarrow i}} \propto 1/d^2$. Beyond a threshold distance d_{crit}, which is set by $w_{\mathrm{f}\rightarrow\mathrm{i}} = w_f$, the photoexcitation rate $w_{\mathrm{f}\rightarrow\mathrm{i}}$ is smaller than the radiative decay rate w_f, so the f line is not affected by photoexcitation, and neither is R. For $d < d_{\mathrm{crit}}$, photoexcitation can suppress the f line and enhance the i line, until the R ratio approaches zero when the UV radiation field is sufficiently strong. To calculate d_{crit}, we use the distance to Her X-1 of $D = 6.6$ kpc (Reynolds et al. 1997), the UV flux $F_{\nu_{f\rightarrow i}}$ measured by Anderson et al. (1994) and Boroson et al. (1996), and we assume a UV point source. Our results are shown in Table 4, which yield $d_{\mathrm{crit}} \sim 10^{12}$ cm. Kahn et al. (2001) used this sort of procedure for a collisionally ionized gas. The value of d_{crit} becomes $\sim 1/2$ of that in Table 4 if we use the $F(\lambda = 1637$ Å$) \sim 0.4 \times 10^{-13}$ erg s^{-1} cm^{-2} Å^{-1} measured by Boroson et al. (1997) at $\phi = 0.66$. This flux is in rough agreement with observations by Boroson et al. (2000) at $\phi = 0.685$–0.764. We attribute this to time-variability associated with both ϕ- and Ψ-phase, and possibly luminosity fluctuations.

Boroson et al. (2000) found that the UV flux peaked at orbital phase $\phi = 0.5$, and interpreted this as the illuminated face of HZ Her. We can use this information to set a limit to the distance between the pulsar and the narrow line region (r_{line}). Since $r_{\mathrm{line}} \lesssim \sqrt{d_{\mathrm{crit}}^2 + r_{\mathrm{L1}}^2}$, and $d_{\mathrm{crit}} > r_{\mathrm{L1}} \sim 3 \times 10^{11}$ cm, we estimate $r_{\mathrm{line}} \lesssim d_{\mathrm{crit}}$, where r_{L1} is the distance between Her X-1 and the L1 Lagrange point. This limit on r_{line}, obtained from photoexcitation, is shown by the vertical line in Figure 7.

3.2. *Limits on the density from thermal and ionization balance*

Because the R ratio is insufficient to quantify the density, we use the ionization parameter ξ instead. The ionization parameter is defined as $\xi = L/n_e r^2$ erg cm s^{-1} (Krolik, McKee, & Tarter 1981), where L is the luminosity, n_e the electron density, and r is the distance from the neutron star to the X-ray line emitting region. The ionization state of an optically thin, photoionization-dominated gas in equilibrium is fully determined by ξ, and by the spectral shape of the ionizing continuum. Assuming thermal and ionization balance, and with the main-on continuum as input, we calculate the charge state distribution for a grid of ξ by use of the XSTAR plasma code (Kallman & McCray 1982). Our XSTAR models and recombination emission calculations (section 5) determine the ξ where the recombination flux from a given ion is significant. For a fixed emission measure (section 6.1), the ξ-values which correspond to the FWHM of the recombination line power of Ne IX, O VII, and N VI Heα lines are $\log_{10}\xi$ =1.3–2.0, 1.0–1.9, and 0.9–1.7, respectively.

To partially account for the existence of optically thick gas in Her X-1, we do not make density estimations with ξ and instead set limits which are more robust. We account for the decrease in number of photons available for photoionization, for the case where 1) the line emission region is optically thin, and 2) the line-of-sight from the line emission region to the neutron star may be optically thick. We do not account for line emission in an optically thick region, hence we do not need a true transfer computation. One large source of uncertainty in the density estimates obtained from ξ is our knowledge of the flux impinging on the line emission region. In Her X-1, the X-ray flux variation with Ψ-phase is associated with large changes of the optical depth in our line-of-sight to the pulsar. Since the optical depth between the pulsar and the line emission region can be $\tau > 0$, we set upper limits to the density from $n_e = Le^{-\tau}/\xi r^2 < L_{\max}/\xi_{\min} r^2$, where $L_{\max}$ is the main-on state, or maximum, X-ray luminosity. We take $\xi_{\min} = 1.0$ for O VII from the T lower limit set in section 3.3, and from the $\xi(T)$ solution from XSTAR. Because $\xi_{\min}$ coincides with the lower end of the FWHM of the O VII Heα recombination line power, our calculations are validated by the data. We use $\xi_{\min}$ and $L_{\max} = 3.8 \times 10^{37} (D/6.6 \text{ kpc})^2$ erg s^{-1} to obtain the density upper limits for O VII shown in Figure 7. The density limits for Ne IX and N VI are $\sim$ 0.50 and $\sim$ 1.3 times those for O VII, respectively. As the density decreases below the limit, τ increases and the ξ of the emission region increases.

3.3. *Radiative Recombination Continuum*

Free electrons recombining with ions produce an RRC width proportional to T. The observed RRC photons correspond to recombination to the K shell. For a photoionized gas, the RRC will be narrow, since $T \ll I$, where I is the ionization energy (Liedahl & Paerels 1996).

The N VII RRC at $\lambda = 18.59$ Å is detected with a $> 10\ \sigma$ confidence, yielding $(6.5 \pm 2.8) \times 10^{-5}$ photons cm^{-2} s^{-1}, and $kT = 3.7 \pm 1.3$ eV (90% confidence). We also detected the O VII RRC at $\lambda = 16.78$ Å with a $\sim 4\ \sigma$ confidence level in the combined short-on and low state data. The O VII RRC is visible in the added spectrum of the low and short-on states (Fig. 3). The O VII RRC normalization is $(2.8^{+3.3}_{-2.5}) \times 10^{-5}$ photons cm^{-2} s^{-1}, and kT is 2–6 eV (this 90% confidence interval is used to set a density limit in section 3.2). The RRC temperatures confirm photoionization is the dominant heating mechanism (Liedahl & Paerels 1996). Other RRC are not detected.

The observed N VII RRC is not far from the expected flux, if compared to N VII Lyα. The N VII ion has the best measured RRC-to-Lyα ratio, which is 0.28 ± 0.14. The hydrogen-like RRC should have $\sim$ 0.75 the flux (Liedahl & Paerels 1996) of the corresponding Lyα flux (see Table 2). Thus, the N VII RRC is close to, but weaker, than the expected strength. For both O VII and N VII, the measured T agree with our XSTAR calculations, within the statistical errors.

A high-temperature component, or a finite optical depth, can explain the weak RRC observed in the narrow line region. An RRC with $T \gtrsim 50$ eV, which may originate in an extended hot corona (section 6.1), would be difficult to distinguish from the continuum. Alternatively, if the optical depth is significant, RRC photons produce ionizations and "fill in" the absorption edges, thereby pumping the recombination lines. However, optical depth effects also imply changes in the Lyα/Lyβ ratios, and perhaps on the Heα r and Lyα lines, which are not observed.

4. SPECTROSCOPY OF THE MAIN-ON STATE

The main-on RGS spectrum is characterized by a bright continuum which has a broad "bump" at $\sim$10–15 Å (Fig. 4). Excess emission near the O VII Heα wavelength is present. We performed a single power-law fit on the spectrum, using the first order data, and we filled the wavelength gap with the second order data.

The RGS spectrum is dominated by a soft continuum component which is distinct from the hard (photon index = 0.87) power-law component observed with EPIC (Ramsay et al. 2002). This hard power-law component does not significantly contribute to the RGS spectrum for $\lambda \gtrsim 8$ Å. For simplicity, we fit the RGS continuum level independently (Table 3). The EPIC PN is consistent with the RGS spectrum at $5 < \lambda < 14$ Å, within the known uncertainties in the calibration.

Centered at the O VII i line wavelength, we observe an excess of emission (see Fig. 5). Due to the noise in this feature, we are not certain if it is composed of a single line or multiple lines, or if it is an emission line at all. However, rebinning reveals a statistically significant emission feature. For reference, we perform a two-Gaussian line fit, assuming the feature is O VII Heα, with $R = 0$ and $G = 4$ (the line ratios observed in the other states). This yields a $\sigma = 3200 \pm 800$ km s^{-1} velocity broadening, but we caution that σ may not have a physical meaning. We search for a feature at the O VIII Lyα wavelength, but the statistics are not sufficient for a detection (see the observed profile in Fig. 8). We set upper limits for the O VIII Lyα and N VII Lyα line fluxes, assuming they have the same velocity broadening as the putative O VII Heα.

We detect a neutral O edge and set a limit on the neutral N edge (see edge data in Table 5). The RGS calibration data in the SAS version 5.3 analysis software does include an instrumental O (oxide) edge. Cold absorption models with solar abundances do not provide acceptable fits. We fit the O edge to obtain an upper limit on the interstellar O I column density of $N_{\rm O\ I} < 4.8 \times 10^{17}$ cm^{-2}, which implies an equivalent H column of $(N_{\rm H})_{\rm eq} < 5.7 \times 10^{20}$ cm^{-2}, if we use the Wilms, Allen, & McCray (2000) solar abundances. A resonant 1s-2p absorption feature from atomic O is detected. This 1s-2p interstellar absorption feature has been observed before in other X-ray binary spectra (Paerels et al. 2001). We set a 90% upper limit for the column $N_{\rm N\ I} < 1.2 \times 10^{17}$ cm^{-2}. The Ne and Mg edges are not detected, but limits cannot be set reliably due to the uncertainty in the continuum in the $\sim$10–15 Å range.

Analysis of the first and second order RGS 1 spectrum does not yield any robust line identifications of individual Fe L transitions. A power-law fit results in negative residuals at 9–10 Å, and positive residuals at 11–15 Å and $\sim$ 7–8 Å(Fig. 4). These residuals do not appear thermal, and they can be described as a broad "bump" at ∼10–15 Å. The "bump" at 10–15 Å was previously identified with Fe L emission (Oosterbroek, Parmar, Martin, & Lammers 1997), but these observations were performed with low-resolution instruments. The high-resolution spectrum obtained by the *Einstein* spectrometer also showed a broad emission feature at 1 keV with low statistical significance (McCray et al. 1982; Vrtilek et al. 1991). The possible nature of this "bump" is discussed in section 6.4.

5. A METHOD TO MEASURE ELEMENTAL ABUNDANCE RATIOS FROM RECOMBINATION EMISSION LINES

The Heα and Lyα emission lines observed in the low and short-on states are modeled to extract the elemental abundance ratios between C, N, O, and Ne. We calculate the C VI Lyα, N VI Heα, N VII Lyα, O VII Heα, O VIII Lyα, and Ne IX Heα line fluxes from a grid of regions which have ξ separated by $\Delta(\log_{10}\xi) = 0.1$. Good ξ-sampling is necessary for an accurate abundance determination because the recombination rates and charge state distribution are sensitive to ξ. To calculate the state of the gas in each region, we run the XSTAR code, using as input the main-on broadband continuum shape. The main-on continuum consists of a 92 eV blackbody, a broken power law which has a break at 18 keV and photon indeces 0.88 and 1.8, and a 24 keV exponential cutoff. This spectrum was measured by dal Fiume et al. (1998), and it is consistent with the EPIC observations. We assume thermal and ionization balance, which is justified due to the short time required for equilibration at the densities of interest (see the limits on the density in section 3.2). Knowledge of the emission measure $EM = \int n_e^2 dV$ as a function of ξ is necessary to measure the elemental abundances, which implies a model dependence. To constrain $EM(\xi)$ from the spectrum, one may choose a single ξ for each ion, such that the radiative recombination flux is maximized, and then calculate the EM for all the ions detected (Sako, Liedahl, Kahn, & Paerels 1999). However, each ion species emits copiously at a broad range of ξ, which must be taken into account to obtain an accurate measure of $EM(\xi)$ and the abundances.

We introduce a method to find the emission measure and the elemental abundances simultaneously. We assume a functional form for $EM(\xi)$ and then test the likelihood of the hypothesis with χ^2. The differential emission measure distribution is well fit with the power-law form

$$DEM(\xi) = \frac{\partial(EM)}{\partial(\log_{10}\xi)} = K\xi^{\gamma}. \qquad (2)$$

The zero-slope $\partial(EM)/\partial(\log_{10}\xi) = 0$, and the commonly assumed $\partial(EM)/\partial\xi = K\ \delta(\xi - \xi_o)$ (this is equivalent to a single ionization parameter), are inconsistent with the observed spectrum, where K, γ, and ξ_o are fit parameters and $\delta()$ is the delta function. We use the recombination rate coefficients calculated by Liedahl (private communication) with the *HULLAC* code (Klapisch et al. 1977). The observed fluxes are fitted using a simplex χ^2-minimization algorithm, with 5 free parameters: the relative abundances, K, and γ. We fit each observation independently, to test the robustness of the method. The results in Table 6 show that 1) consistent fits can be found by the algorithm, 2) the phenomenological equation (2) provides an excellent fit to the RGS spectra in the low state and a marginal fit in the short-on state, 3) the results are sensitive to the shape of the ionizing spectrum, which can be seen by comparing the results obtained with the main-on spectrum and with a 20 keV bremsstrahlung spectrum, and 4) the N/O abundance ratio is at least four times the solar value, while the C/O and Ne/O ratios indicate that both carbon and oxygen are depleted with respect to neon. The marginal fit of the short-on spectrum may be due to a physical emission measure which differs from a power-law distribution. The large (N VII + N VI)/(O VIII + O VII) ratio is evident in the spectrum on Figure 2.

We discuss the validity and limitations of the method. The method is robust insofar the $DEM(\xi)$ is well-covered in ξ by the observed ions, and because the emission measure is not extrapolated to other ξ. Also, it relies on the observed absence of optical depth or resonance scattering effects in the helium-like ion line ratios. The abundance ratios depend on the XSTAR plasma code assumptions, which may introduce systematic errors that are not addressed in this paper. We have used a 20 keV bremsstrahlung as a benchmark to test the dependence of our results to the ionizing spectrum, and we do not observe an improvement in the χ^2 of the fit; albeit the C/O and N/O abundance ratios are lower than with the main-on spectrum. XSTAR is run at $n_e = 10^{10}$ cm^{-3}, a regime for which three-body recombination of the observed ions is unimportant, and in the optically thin case. For $n_e < n_{\rm crit}$, the recombination line fluxes depend only weakly on n_e. The value of $n_{\rm crit}$ depends on the ion, and is roughly $n_{\rm crit} \sim 10^{17}$ cm^{-3} for O VIII (Kallman & Bautista 2001). The low-density assumption holds for the narrow line region (Fig. 7). We assume Gaussian statistics since there are > 44 photons in each of the lines used for the abundance ratio measurement. We excluded Ne X Lyα from the fit since it is detected with low statistical significance, but our fits are consistent with the observed limits.

Models of the Her X-1 UV spectrum roughly agree with the abundances we measure. CNO-processing abundances were also evidenced by the N V/O VI line ratio observed in the UV (Boroson et al. 1997), which was compared to spectral models of a photoionized accretion disk (Raymond 1993). We crudely estimate an abundance ratio N/O ~ 6.0 times solar from the observed discrepancy of the N V/O VI line flux ratio with the CNO-disk model. However, the N V/O V ratio yields N/O ~ 2.6 times solar. A C IV/O V ratio depleted below the solar abundance value was also observed by Boroson et al. (1997). Our X-ray spectral measurements are more reliable than the UV ones because they are less sensitive to radiation transfer effects, and because the X-ray line fluxes have been fitted consistently with the DEM.

The functional form of $DEM(\xi)$, through the K and γ parameters, contains information on the gas density and geometry. A power-law dependence of the $DEM(\xi)$ is expected in some simple geometries such as: a uniformly filled sphere, an optically-thin disk atmosphere with a scale height $H \propto r^n$, and an illuminated slab with $\rho(z) \propto \rho_o e^{-z/z_o}$. A full interpretation of the K and γ parameters is outside the scope of this paper.

6. DISCUSSION

A new, X-ray narrow line component in the Her X-1 system has been discovered. We discuss the possibility that this narrow line region is the illuminated face of HZ Her, or an accretion disk atmosphere and corona. Our elemental abundance measurements serve to quantify the CNO processing products from HZ Her. We discuss the connection between the CNO products and the history of the binary system.

The main-on spectrum shows a peculiar continuum feature and possibly a broad emission line component. We discuss the physical plausibility of such a broad line component.

6.1. *Recombination emission from the disk atmosphere or the illuminated companion*

We investigate the nature of the photoionized gas emitting narrow X-ray lines during the low and short-on states. The UV line emission consists on a narrow ($\sigma \sim 80\ \mathrm{km\,s^{-1}}$) line component, which is likely to originate on the illuminated face of HZ Her, plus a broader ($\sigma \sim 300$ km s^{-1}) component, attributable to the accretion disk (Boroson et al. 2000). Similar dynamical components in the X-ray narrow line region would not be distinguished with the RGS energy resolution alone.

The limits found on the density and location of the narrow line region are shown in Figure 7. We set the density lower limit of the O VII region with the emission measure calculated from the line flux. The lower limit to the root-mean-square of the density is $(n_{\rm rms})_{\rm min} = \sqrt{EM/V_{\rm max}}$, where the maximum volume $V_{\rm max} = \frac{4}{3}\pi r^3$. The R-ratio density thresholds listed in section 3.1 indicate that, within much of the allowed region in Figure 7, the $2^3S \to 2^3P$ electron-impact excitation rate is larger than the photoexcitation rate. Radius limits for the putative Kepler orbits are obtained from the circularization radius and from upper limits to the velocity broadening (Fig. 7). However, a disk larger than the circularization radius ($\sim 1.7\times10^{11}$ cm) was deduced from UV and optical light curves (Howarth & Wilson 1983).

An extended, photoionized accretion disk atmosphere and corona may be responsible for the observed recombination emission and the underlying continuum. Model calculations (Jimenez-Garate, Raymond, Liedahl, & Hailey 2001) show that a centrally illuminated, photoionized accretion disk would develop an extended, Compton-temperature coronal structure, and a more compact, X-ray recombination-emitting atmospheric layer (see Fig. 9). We first interpret the behavior of the Her X-1 spectrum in terms of this picture. The line fluxes observed are within a factor of two (scaled by the Her X-1 luminosity and disk radius) of the photoionized accretion disk atmosphere model results, and the line ratios are all within a factor of unity of model values. The model density of the helium-like ion region is 10^{13}–10^{14} cm^{-3} if the disk radius is $r \sim 5 \times 10^{10}$ cm, which are inside the limits on Figure 7. If the X-ray line velocity broadening can be resolved, this would support the accretion disk emission hypothesis (the evidence is marginal from the RGS, see Table 2). The line emitting disk atmosphere is optically thin towards most lines of sight, although its flattened geometry allows it to partially shield itself from the pulsar ($e^{-\tau} \lesssim 0.1$). The soft X-ray continuum is dominated by Compton scattering in the disk corona during the low and short-on states. The optical depth of both atmosphere and corona decreases as the 1) radius increases, and as 2) the height above the disk mid-plane increases. At high inclination, the interior of the disk is obscured by the outer disk edge. As the disk precesses out of its edge-on configuration, parts of the disk which are close to the neutron star are less obstructed, and deeper layers of the disk come into view, increasing both the atmospheric line flux and the Compton scattered light from the corona. This may explain the spectral evolution observed from the low to the short-on state. As the disk inclination decreases further in the main-on state, the pulsar comes into view and overwhelms the narrow line flux from the disk. The duration of X-ray eclipse ingress or egress at the low and short-on states is measured in the 1500 s to 3 hr range (Leahy 1995; Choi, Seon, Dotani, & Nagase 1997), corresponding to source radii of 4×10^{10} cm to 3×10^{11} cm. Eclipses of the X-ray lines are very likely to occur, since similar radii estimates have been obtained from the eclipse of the broad UV line emission region. About $\sim 0.1\times10^{-13}$ erg s^{-1} cm^{-2} Å^{-1} or ~ 6 % of the UV continuum, together with the broad C IV and N V emission lines, are gradually eclipsed, indicating a $\sim 10^{11}$ cm UV emission region (Boroson et al. 2000). Eclipse measurements, together with the X-ray spectrum and its variability, and the photoionized disk models, lend support to the disk atmosphere and corona origin of the X-ray emission during the low and short-on states.

The spectrum of the accretion disk corona (ADC) source 4U 1822-371 (Cottam et al. 2001) is very similar to the Her X-1 low and short-on state spectra, confirming that ADC sources provide an edge-on view of the disk and supporting the idea that the accretion disk in Her X-1 is precessing.

The variability of the X-ray line emission with Ψ-phase and ϕ-phase, combined with the predicted disk inclination from the Scott, Leahy, & Wilson (2000) model, suggests that at least some of the X-ray line flux originates on HZ Her. The total line emission flux in the RGS band at phase $\Psi = 0.60$ is two times larger than during phase $\Psi = 0.26$, at approximately the same orbital phase ($\phi \sim 0.5$). Taking the predicted outer disk inclination from the Scott, Leahy, & Wilson (2000) model, we have drawn the schematic in Figure 10 (Model B). If the line emission originates in an accretion disk atmosphere and corona, the line flux should increase as more of the disk's area comes into view. If the line emission originates in HZ Her, the line flux should increase as the visible area of HZ Her increases. If the outer disk inclination predicted by the model of Scott, Leahy, & Wilson (2000) is correct, then some of the line emission in the short-on must be coming from the photoionized face of HZ Her. If the X-ray line emission originates on HZ Her, it should vary with orbital phase in a way similar to the UV continuum flux (Boroson et al. 2000). Some dependence of the narrow line flux on ϕ-phase is hinted by the main-on observation. The upper limits to the narrow lines which we derive for the main-on observation at $\phi \sim 0.2$, are below the line fluxes in the low and short-on states, which were observed at $\phi \sim 0.5$. However, this may be due to a Ψ-phase dependence only. Observations at various orbital phases and similar Ψ-phase, during the low and short-on states, can disentangle the companion and disk components.

However, model values of the outer disk precession phase differ (see Models A and B in Fig. 10). Model B (Scott, Leahy, & Wilson 2000) yields a precession phase which lags by $\Delta\Psi \sim 0.16$ the phase from model A (Gerend & Boynton 1976; Howarth & Wilson 1983), which fits the optical and UV lightcurves. In model A, the maximum disk opening angle to our line-of-sight occurs during the main-on and short-on peaks, at $\Psi = 0.13$ and 0.63. Model A favors the interpretation that the line emission originates in a disk atmosphere and corona, since the projected disk opening angle and the line fluxes during the short-on are larger than during the low state.

6.2. *New constraints on the X-ray binary evolution from the derived CNO abundances*

The unusually high N/O abundance ratio and the low C/O and O/Ne ratios we have measured are the result of H-burning by the CNO-cycle in the core of a massive star. The CNO-cycle produces N and depletes O and C, until H is exhausted (Clayton 1983, and references therein). Evidence for CNO processing in the Her X-1 system was previously obtained from UV spectra, which show N-enrichment and C-depletion (Boroson et al. 1997, see section 5). Evolution models of an isolated star with a mass comparable to HZ Her cannot explain the observed abundances, even after the end of the H-burning phase. A mechanism to enrich the HZ Her envelope with CNO-processed material is required, and such a mechanism is likely linked to the presence of a companion. The CNO abundances thus provide a stringent constraint on the evolution of the binary system.

We compare the measured CNO yields with those in an isolated intermediate-mass star. Stellar evolution models (Schaller, Schaerer, Meynet, & Maeder 1992) of an isolated 2.5 $M_{\odot}$ star show a N/O abundance ratio enhancement of 2.6 to 2.8 times the zero-age N/O ratio, a C/O ratio of 0.60 to 0.70 times its zero-age value, and an unchanged Ne/O ratio. The quoted range corresponds to zero-age solar ($Z = 0.02$) and sub-solar ($Z = 0.001$) metallicities, at the end of the H-burning phase, after $\sim 5.8 \times 10^8$ yr. The N-yield and the C-depletion are maximized near the end of the H-burning phase. The N-yield increases with stellar mass. For example, a 4.0 $M_{\odot}$ star produces a N/O ratio which is 4.0 times its zero-age value (Schaller, Schaerer, Meynet, & Maeder 1992). Models of the evolution of an isolated ~ 2.5 $M_{\odot}$ star under-predict the observed N-yield in HZ Her.

The observed N-enrichment with RGS cannot be attributed to systematic uncertainties in the data, nor could we attribute it to a dependence on the photoionization equilibrium calculations. The systematic errors due to fitting of the emission lines and the continuum are $< 25\%$ (section 3). Any RGS calibration errors are ~ 10 % where most of the emission lines have been measured, and even the worst-case O I edge calibration error scenario implies a $\lesssim 35\%$ error in the O VII Heα line flux, since $\tau_{\mathrm{O\ I}} \sim 0.3$. If we propagate a $\pm 35\%$ uncertainty in the O VII Heα flux through the abundance extraction calculation, the N/O ratio changes by $< 35\%$. The measured abundance ratios depend on the shape of the ionizing spectrum, which affects the equilibrium state of the plasma (section 5). The changes in the 0.5-10 keV continuum from the main-on state to the low and short-on states are well-fit with a varying N_H on a constant-slope power-law (Ramsay et al. 2002). Most of the line emission should be generated by reprocessing of the direct pulsar (main-on) continuum, which consists of a power-law with a cutoff. Taking a 20 keV bremsstrahlung ionizing spectrum still yields a N/O > 4.0 times the solar value, and underabundant C and O with respect to Ne (Table 6), so a systematic difference in the plasma equilibrium state cannot, by this measure, explain the CNO abundances.

The detection of CNO-processed material is validated by measurements of the (C + N + O)/Ne abundance ratio. The (C + N + O) abundance sum is conserved by the CNO-cycle, so the sum should be near the solar value. We measure the (C + N + O)/Ne ratio for the two best fits in Table 6, obtaining 0.74 ± 0.28 times solar with the main-on continuum model, and 0.45 ± 0.19 times solar with the 20 keV bremsstrahlung model.

To explain the observed abundances in HZ Her, a mechanism is required to transfer CNO-processed material to the envelope. One possibility is that enhanced mixing and significant mass loss from the HZ Her envelope enrich it with CNO products from the core. The stellar core is richer in CNO products: for the 2.5 $M_{\odot}$ example above, the abundance ratios are C/O ~ 0.04, N/O ~ 10, and Ne/O ~ 10 times the zero-age values (Schaller, Schaerer, Meynet, & Maeder 1992). These abundances have not reached the equilibrium CNO values, which have higher N-yields. The CNO products must have been efficiently transported from the core to the surface. However, the stellar core contains only ~ 0.1 times the mass of the star. The shedding of a N-poor stellar envelope though Roche-lobe overflow may explain the observed N-enrichment. Intermediate-mass companions may survive super-Eddington accretion, as evidenced by observations of the Cygnus X-2 mass donor (King & Ritter 1999), and by models of the evolutionary track of that binary system (Podsiadlowski & Rappaport 2000). The mixing of the core's CNO products with the envelope gas is needed to explain the observations, but that may complicate the calculation of the CNO burning rates, which depend on the concentration of nuclear species in the core. Another possibility is that the CNO-processed material was transferred from the neutron star progenitor onto HZ Her. A massive neutron star progenitor can readily produce the CNO elements in a $\sim 10^7$ yr timescale, and would not require HZ Her to be highly evolved. The presence of a companion has likely affected the elemental composition of HZ Her, which presents a challenge to our understanding of the evolution of the binary.

It is highly likely that the evolutionary state of the companion stars in low- and intermediate-mass X-ray binaries is more evolved than had previously been anticipated. This has been shown by modeling the evolution paths of 100 sample systems, from a grid of initial stellar masses and periods (Podsiadlowski, Rappaport, & Pfahl 2002). These models show that many LMXB evolve from intermediate-mass binaries, so that many LMXB should be H-deficient and He-enriched, and the surface composition of the evolved secondaries should show evidence of CNO processing. The CNO abundances we find in Her X-1 are consistent with this basic picture. The determination of the age of HZ Her, its zero-age mass, and the initial period of the binary can be better addressed by binary evolution models now that the CNO abundances have been measured (Podsiadlowski, Rappaport, & Pfahl 2002, and private communication).

6.3. *The physical plausibility of a broad line component*

We make the case that a broad line region is physically plausible if it is neighboring the Her X-1 magnetopause, and we point out that broad recombination lines have been observed previously in another accreting X-ray pulsar.

A low-mass, compact X-ray binary system, 4U 1626-673, contains a pulsar which is accreting from a white dwarf, and it exhibits prominent recombination emission lines (Schulz et al. 2001). The *Chandra* High-Energy Transmission Grating detected the Ne X Lyα, Ne IX Heα, O VIII Lyα, and O VII Heα lines with FWHM $\sim$ 2500 km s^{-1}, and it resolved them into two distinct peaks, suggesting a disk origin. If the broadening is due to the orbital velocity, the material would be located on the disk, exterior to the pulsar magnetopause (Schulz et al. 2001). 4U 1626-673 has a cyclotron line with 0.85 times the energy than the corresponding line in Her X-1, a 3.4 times larger corotation radius, and broad lines with $\sim 1/20$th the flux of Her X-1 (the unabsorbed X-ray flux from 4U 1626-673 is $\sim 1/36$th the Her X-1 main-on flux). It is possible for broad recombination lines to be associated with the accretion flows around X-ray pulsars, which have $B \sim 10^{11}$–10^{12} G.

In Her X-1, from the putative O VII Heα broad lines, we estimate that the emission region would be inside the 4.5×10^8 cm $< r < 3 \times 10^9$ cm boundary. We assume the velocity broadening is due to circular Kepler orbits, and that $\sim$90% of the emission in the O VII Heα Gaussian line fit is enclosed within $v = \pm 2\sigma$ of the centroid. The estimated inner disk radius is just larger than the corotation radius $r_{\rm co} = (GMP_{\rm pulse}^2/4\pi^2)^{1/3} = 1.9 \times 10^8$ cm, and is near the Alfvèn radius (Ghosh & Lamb 1979).

The putative O VII Heα broad line luminosity would imply that a fraction of order $\sim 10^{-1}$ of the luminous energy of the pulsar is directed towards the line emission region. Emission measure calculations allow us to set a $n_e > 10^{14}$ cm^{-3} density lower limit, from the radius upper limit above. This implies that there would be significant line opacity effects, which would have to be included in the photoionization equilibrium calculations. Hypothetically, a nearly Compton-thick region enshrouding the pulsar, of radius of a few times 10^8 cm, may be illuminating an inner accretion disk, which then emits the broad recombination lines (Fig. 9). To illustrate, a shell of Compton-thick gas at $r \sim 10^8$ cm, and with $\Delta r \sim 10^7$ cm thickness requires $n_e \sim 10^{17}$ cm^{-3} and $\log_{10}\xi \sim 4$, which indicates the plasma would be fully ionized, except perhaps for iron. An illuminated disk region of radius $r \sim 3 \times 10^9$ cm would have $n_e \sim 4 \times 10^{17}$ cm^{-3}, which corresponds to the ξ for maximum line power, and taking $\Delta r \simeq 0.5r$ and volume $V = 2\pi r h \Delta r$, its height would be $h \sim 10^3$ cm.

The duration of eclipse ingress and egress varies during the Her X-1 main-on state, and it yields source size estimates in the 5×10^8 cm to 3×10^9 cm range, albeit the smaller estimate may be affected by the HZ Her atmosphere (Leahy 1995; Leahy & Yoshida 1995; Day, Tennant, & Fabian 1988).

6.4. *The 10–15 Å "bump"*

The origin of the 10–15 Å "bump" observed in the main-on state is unclear. We describe three possible explanations for this "bump". The first possibility is that the "bump" is a superposition of Fe L emission lines with a velocity broadening as in O VII Heα. The blended transitions may range from Fe XVII through Fe XXIV, at 10–17 Å. However, photoionized gases have weak Fe L emission relative to hydrogen-like and helium-like ions of low- and mid-Z elements (Liedahl et al. 2001). If the "bump" is Fe L emission, it could be due to shock-heated gas in the magnetopause, although the G line ratio from O VII Heα is not consistent with collisional heating.

The EPIC data suggest that the "bump" results from the overlap of the pulsar power-law continuum with a reprocessed, soft component. Shortward of $\lambda \sim 6$ Å, for the hard power-law, the pulse profile consists of sharply peaked pulses, indicating a $\lesssim 10^8$ cm emission region. Longward of $\lambda \sim 14$ Å, the pulse profile is nearly sinusoidal, indicating a $\sim 10^9$ cm emission region (Ramsay et al. 2002). The soft component is not a Planck spectrum.

A third possibility is that we are observing a blended and broad Fe L resonance absorption complex. Fe L absorption is not suppressed in photoionized gases. In this case, absorption lines from hydrogenic and helium-like ions should also be observed.

7. CONCLUSIONS

We analyzed the high-resolution X-ray spectra of Her X-1 obtained with the *XMM-Newton* RGS from three observations performed at distinct states of its 35 d cycle.

We detect narrow recombination emission lines during the low and short-on states of Her X-1. Emission lines are detected from C VI, N VI, N VII, O VII, O VIII, Ne IX, and perhaps Ne X, plus weak RRC of O VII and N VII, which indicate the gas is photoionized. The velocity broadening of the lines is at the resolution limit of the RGS (e.g. $\sigma \lesssim 260$ km s^{-1} for N VII Heα). In the 5–38 Å band, the low and short-on states have power-law continua, while the main-on continuum exhibits excess emission in the $\sim$ 10–15 Å band. The continuum flux during the short-on is twice as during the low state, a tendency that is followed by most line fluxes as well.

We measure the abundance ratios among C, N, O, and Ne with the following method: we use a power-law emission measure distribution, in conjunction with a grid of XSTAR plasma models, and the *HULLAC* recombination rates, to fit the narrow line fluxes, and obtain the abundance ratios with the emission measure parameters simultaneously. We perform the measurements for the low and short-on state data separately, and we obtain consistent results with acceptable χ^2 (Table 2). The enrichment of nitrogen relative to oxygen, of more than four times the solar values, plus the depletion of C and O with respect to Ne, indicate extensive H-burning in a massive star. The measured abundances require a mechanism for transferring the CNO-processed material onto the HZ Her envelope. This mechanism is likely linked to the presence of a companion, providing an additional constraint on the evolution of the X-ray binary.

We use spectroscopic analysis and models to set limits on the density and location of the narrow line region.

These limits (Fig. 7) provide important clues on the nature of the line emission region. We assume thermal and ionization balance to set upper limits on the density, and we use the emission measure derived from the line fluxes to set lower limits on the density. If the line velocity broadening is due to Kepler motion, we may set bounds to the orbital radii. We use the Heα line ratios and UV photoexcitation calculations to set upper limits to the radius enclosing the region. The low RRC temperatures ($30,000 < T < 60,000$ K) allow us to validate our density upper limits and the photoionization equilibrium models.

The narrow line region may be identified with an accretion disk atmosphere and corona, or with the illuminated face of HZ Her. The evidence for the disk identification relies on the modeled structure and spectra from a photoionized disk (Jimenez-Garate, Raymond, Liedahl, & Hailey 2001), which agree with the limits set on the density (10^{13}–10^{14} cm^{-3}). The unresolved velocity broadening indicates the outermost ($r \sim 5\times10^{10}$ cm) radii of the disk dominate the emission, in agreement with the models, while fluxes of the observed hydrogen and helium-like lines are within a factor of two of the calculations. Observations from previous missions of the eclipse ingress and egress reveal an emission region which can match the size of the disk and its corona. The flux variation with orbital phase and with 35 d phase, on the other hand, favors a contribution from the illuminated face of HZ Her to the narrow line emission.

The variability of the Her X-1 spectrum lends support to the precession of the accretion disk. Regions with contrasting dynamical properties are coming into view at different 35 d phases. Notably, Her X-1 exhibits an ADC-like spectrum during low and short-on states, indicating an edge-on disk, while during main-on states, the spectrum is dominated by the continuum, due to a disk inclination which exposes the pulsar to our line of sight.

We detect an excess of emission centered on the O VII Heα i line wavelength during the main-on state. If this feature is due to the O VII Heα i and r lines, their velocity broadening would be in the order of 10^3 km s^{-1}. Similarly broad, yet double-peaked lines, have to date only been observed from the accreting pulsar in 4U 1626-67 (Schulz et al. 2001). The observed emission emission feature is noisy, but if it is real, it may be due to emission in the inner accretion disk, near the pulsar magnetopause.

We are grateful for the input provided by Duane Liedahl. We thank Saul Rappaport, John Raymond, and Maurice Leutenegger for engaging in fruitful discussions. We thank the members of the RGS instrument team and the MIT CXC and HETG groups for their support. We acknowledge our use of the public data which was made promptly available by the *RXTE* all-sky monitor team.

REFERENCES

Anderson, S. F., Wachter, S., Margon, B., Downes, R. A., Blair, W. P., & Halpern, J. P. 1994, ApJ, 436, 319
Arnaud, K.A. 1996, in ASP Conf. Ser. 101, Astronomical Data Analysis Software Systems V, ed. G. Jacoby, & J. Barnes (San Francisco: ASP), 17
Baushev, A. N. & Bisnovatyi-Kogan, G. S. 1999, Astronomy Reports, 43, 241
Bautista, M. A. & Kallman, T. R. 2000, ApJ, 544, 581
Boroson, B., Vrtilek, S. D., McCray, R., Kallman, T., & Nagase, F. 1996, ApJ, 473, 1079
Boroson, B., Blair, W. P., Davidsen, A. F., Vrtilek, S. D., Raymond, J., Long, K. S., & McCray, R. 1997, ApJ, 491, 903
Boroson, B., Kallman, T., Vrtilek, S. D., Raymond, J., Still, M., Bautista, M., & Quaintrell, H. 2000, ApJ, 529, 414
Cann, N. M., & Thakkar, A. J. 1992, Phys. Rev. A, 46, 9, 5397
Chiang, J. 2001, ApJ, 549, 537
Choi, C. S., Seon, K. I., Dotani, T., & Nagase, F. 1997, ApJ, 476, L81
Clayton, D. D. 1983, Principles of Stellar Evolution and Nucleosynthesis (Chicago: University of Chicago Press)
Cottam, J., Sako, M., Kahn, S. M., Paerels, F., & Liedahl, D. A. 2001, ApJL, 557, L101
dal Fiume, D. et al. 1998, A&A, 329, L41
Day, C. S. R., Tennant, A. F., & Fabian, A. C. 1988, MNRAS, 231, 69
Deeter, J. E., Boynton, P. E., Miyamoto, S., Kitamoto, S., Nagase, F., & Kawai, N. 1991, ApJ, 383, 324
Deeter, J. E., Scott, D. M., Boynton, P. E., Miyamoto, S., Kitamoto, S., Takahama, S., & Nagase, F. 1998, ApJ, 502, 802
Drake, G. W. F. 1971, Phys. Rev. A, 3, 908
Gabriel, A. H. & Jordan, C. 1969, MNRAS, 145, 241
Gerend, D. & Boynton, P. E. 1976, ApJ, 209, 562
Giacconi, R., Gursky, H., Kellogg, E., Levinson, R., Schreier, E., & Tananbaum, H. 1973, ApJ, 184, 227
Ghosh, P. & Lamb, F. K. 1979, ApJ, 232, 259
Houck, J. C. & Denicola, L. A. 2000, in ASP Conf. Ser. 216, Astronomical Data Analysis Software and Systems IX, ed. N. Manset, C. Veillet, & D. Crabtree (San Francisco: ASP), 591
Howarth, I. D. & Wilson, B. 1983, MNRAS, 202, 347
Jimenez-Garate, M. A., Raymond, J. C., Liedahl, D. A., & Hailey, C. J. 2001, ApJ, 558, 448
Kahn, S. M., Leutenegger, M. A., Cottam, J., Rauw, G., Vreux, J.-M., den Boggende, A. J. F., Mewe, R., & Güdel, M. 2001, A&A, 365, L312
Kallman, T. & Bautista, M. 2001, ApJS, 133, 221
Kallman, T. R. & McCray, R. 1982, ApJS, 50, 263
King, A. R. & Ritter, H. 1999, MNRAS, 309, 253
Klapisch, M., Schwab, J. L., Fraenkel, J. S., & Oreg, J. 1977, Opt. Soc. Am., 61, 148
Krolik, J. H., McKee, C. F., & Tarter, C. B. 1981, ApJ, 249, 422
Leahy, D. A. 1995, ApJ, 450, 339
Leahy, D. A. & Yoshida, A. 1995, MNRAS, 276, 607
Liedahl, D. A. & Paerels, F. 1996, ApJ, 468, L33
Liedahl, D. A. 1999, in X-ray Spectroscopy in Astrophysics, EADN School proceedings, ed. J. A. van Paradijs, & J. A. M. Bleeker (Amsterdam: Springer), 189
Liedahl, D. A., Wojdowski, P., Jimenez-Garate, M. A., & Sako M. 2001, in ASP Conf. Ser. 247, Spectroscopic Challenges of Photoionized Plasmas, ed. G. Ferland, & D. W. Savin (San Francisco: ASP), 417
McCray, R. A., Shull, J. M., Boynton, P. E., Deeter, J. E., Holt, S. S., & White, N. E. 1982, ApJ, 262, 301
McLaughlin, B. M., & Kirby, K. P. 1998, J. Phys. B: At. Mol. Opt. Phys., 31, 4991
Mewe, R. & Schrijver, J. 1978, A&A, 65, 99
Oosterbroek, T., Parmar, A. N., Martin, D. D. E., & Lammers, U. 1997, A&A, 327, 215
Paerels, F. et al. 2001, ApJ, 546, 338
Petterson, J. A. 1975, ApJ, 201, L61
Petterson, J. A., Rothschild, R. E., & Gruber, D. E. 1991, ApJ, 378, 696
Podsiadlowski, P., Rappaport, S., & Pfahl, E. D. 2002, ApJ, 565, 1107
Podsiadlowski, P. & Rappaport, S. 2000, ApJ, 529, 946
Porquet, D., Mewe, R., Dubau, J., Raassen, A. J. J., & Kaastra, J. S. 2001, A&A, 376, 1113
Porquet, D. & Dubau, J. 2000, A&AS, 143, 495
Ramsay G., Zane S., Jimenez-Garate M., den Herder J., & Hailey C., 2002, MNRAS, submitted
Raymond, J. C. 1993, ApJ, 412, 267
Reynolds, A. P., Quaintrell, H., Still, M. D., Roche, P., Chakrabarty, D., & Levine, S. E. 1997, MNRAS, 288, 43
Sako, M., Liedahl, D. A., Kahn, S. M., & Paerels, F. 1999, ApJ, 525, 921
Schaller, G., Schaerer, D., Meynet, G., & Maeder, A. 1992, A&AS, 96, 269
Schreier, E., Levinson, R., Gursky, H., Kellogg, E., Tananbaum, H., & Giacconi, R. 1972, ApJ, 172, L79

Schulz, N. S., Chakrabarty, D., Marshall, H. L., Canizares, C. R., Lee, J. C., & Houck, J. 2001, ApJ, 563, 941
Scott, D. M. & Leahy, D. A. 1999, ApJ, 510, 974
Scott, D. M., Leahy, D. A., & Wilson, R. B. 2000, ApJ, 539, 392
Tananbaum, H., Gursky, H., Kellogg, E. M., Levinson, R., Schreier, E., & Giacconi, R. 1972, ApJ, 174, L143
Truemper, J., Pietsch, W., Reppin, C., Voges, W., Staubert, R., & Kendziorra, E. 1978, ApJ, 219, L105
Vrtilek, S. D., McClintock, J. E., Seward, F. D., Kahn, S. M., & Wargelin, B. J. 1991, ApJS, 76, 1127
Wilms, J., Allen, A., & McCray, R. 2000, ApJ, 542, 914
Wilson, R. B., Scott, D. M., & Finger, M. H. 1997, AIP Conf. Proc. 410, Proceedings of the Fourth Compton Symposium, ed. C. D. Dermer, M. S. Strickman, & J. D. Kurfess (New York: AIP Press), 739

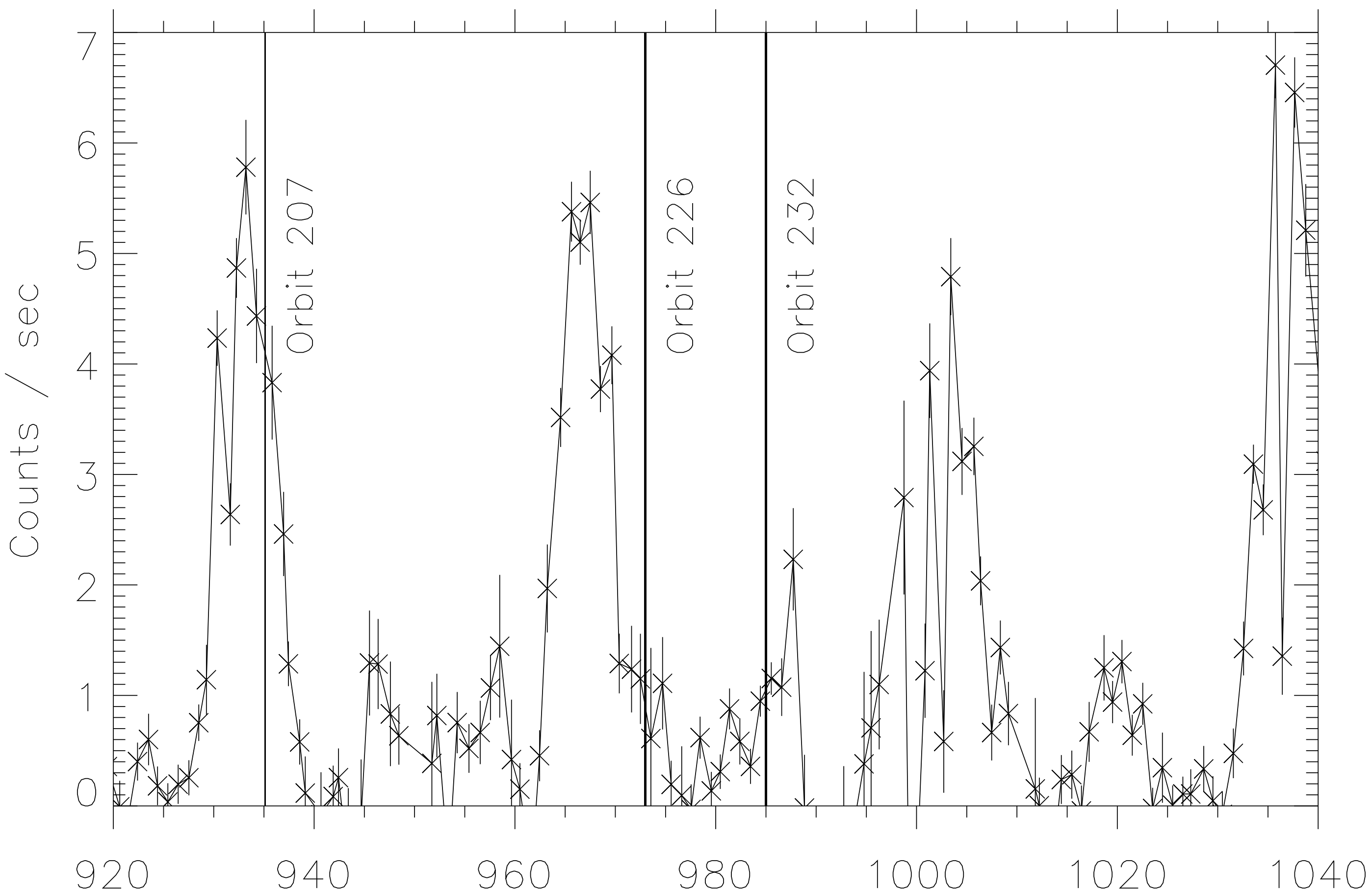

FIG. 1.— Light curve obtained with the *RXTE* all-sky monitor.

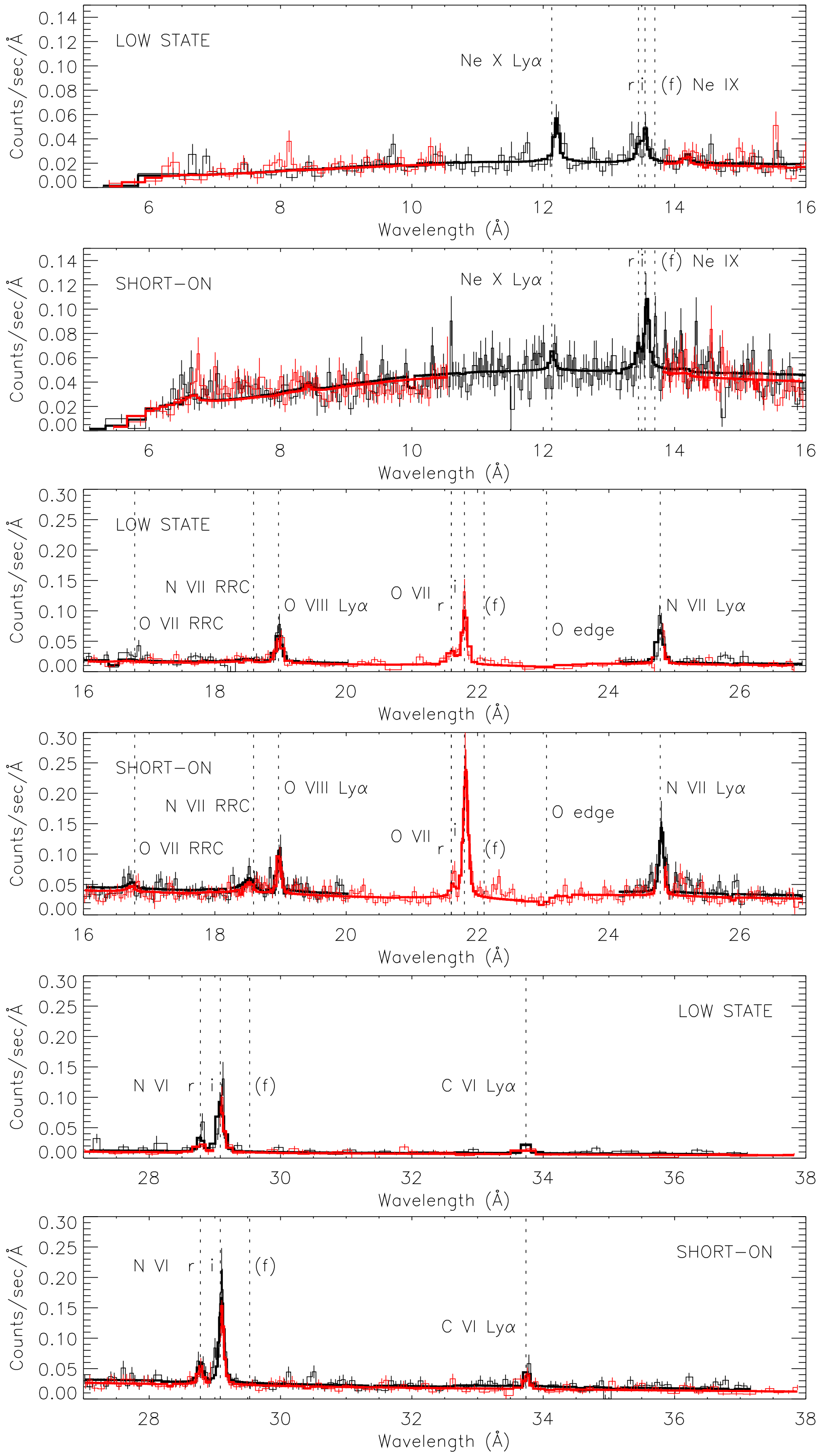

FIG. 2.— High-resolution spectra obtained with RGS 1 (red) and RGS 2 (black), and phenomenological fits (thick-lines). The low state (13 ks) and short-on state (12 ks) observations are shown on adjacent panels. The spectra have been rebinned adaptively.

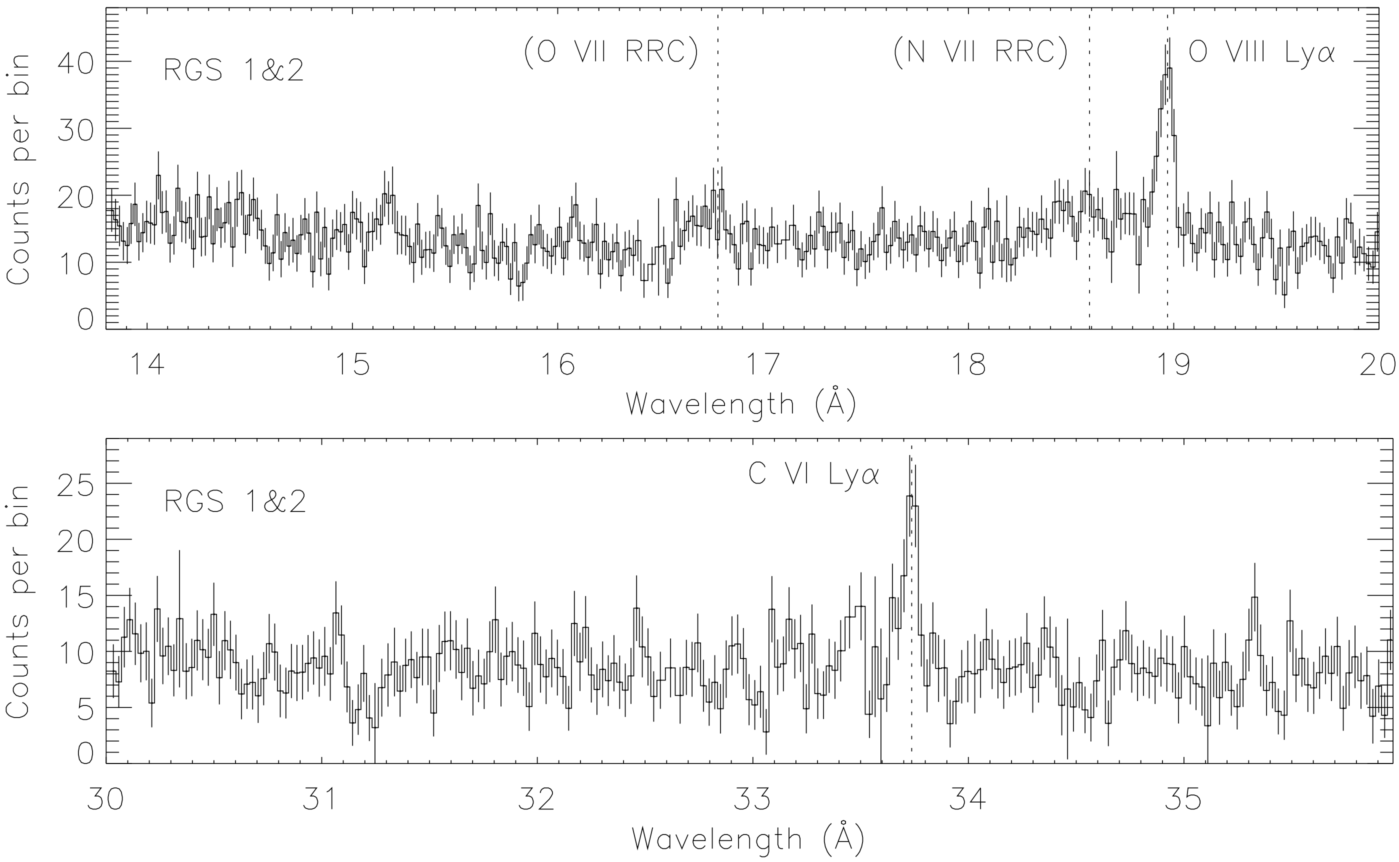

FIG. 3.— Summed RGS spectra of both low-state and short-on data, which highlight the observed RRC of O VII and N VII, and C VI Lyα. The bin size is 21 and 27 mÅ for the top and bottom frame, respectively. The line spread function is different for each RGS and is not corrected on these spectra.

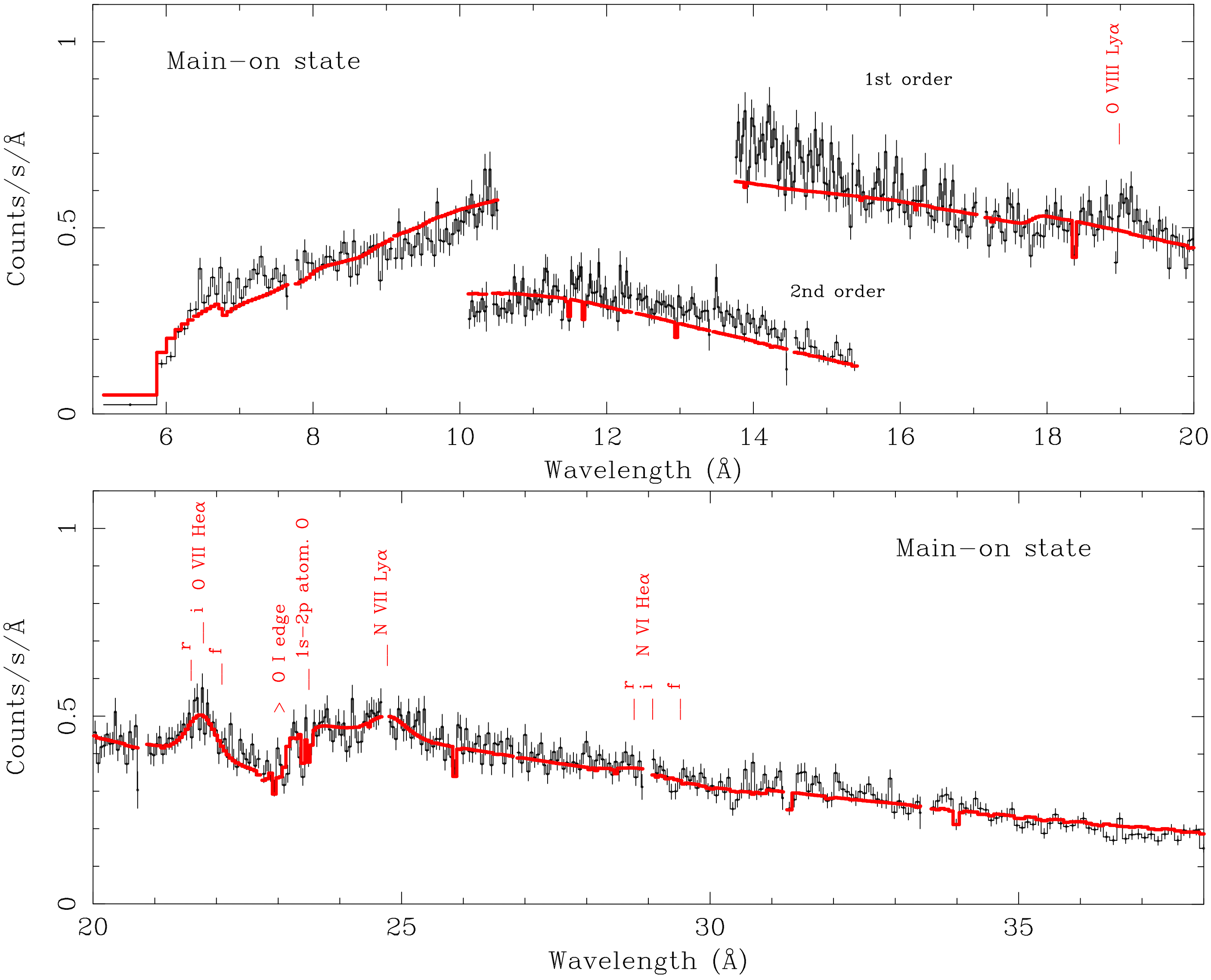

FIG. 4.— High-resolution spectrum with RGS 1 for the main-on state observation (11 ks), plus a phenomenological model fit (thick-line). Both first and second order spectra are shown in the upper and lower part of the figure, respectively.

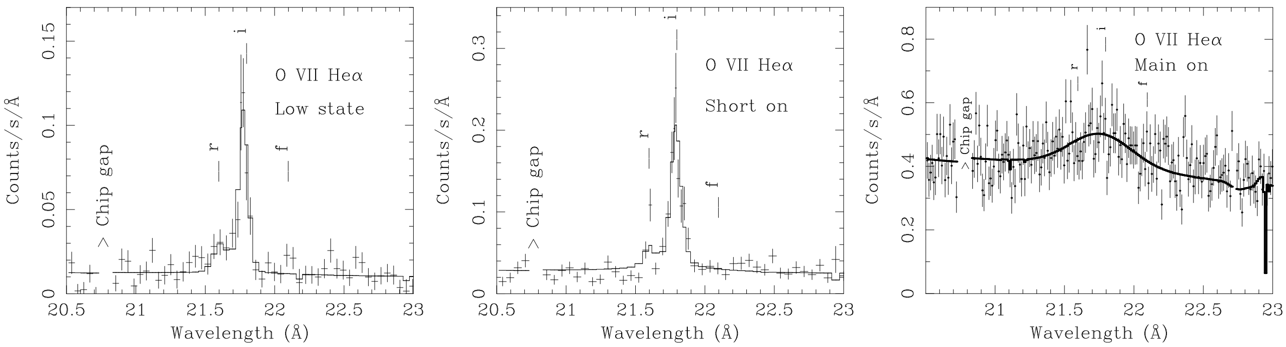

FIG. 5.— The evolution of the O VII emission line complex with 35 d phase. The intercombination (i) and resonance (r) lines are present in the low and short-on states. A complex, broad structure during the main-on is plotted at full resolution. RGS 1 data (symbols) and fits (solid lines) are shown.

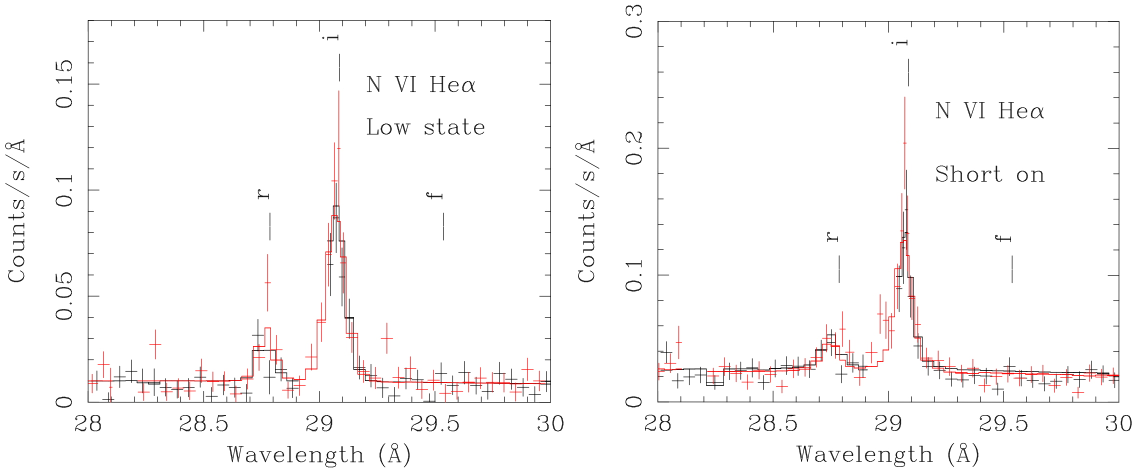

FIG. 6.— The evolution of the N VI emission line complex with 35 d phase. The intercombination (i) and resonance (r) lines are present in both low and short-on states. RGS 1 data (black symbols), RGS 2 data (red symbols), and the respective fits (solid lines), are shown.

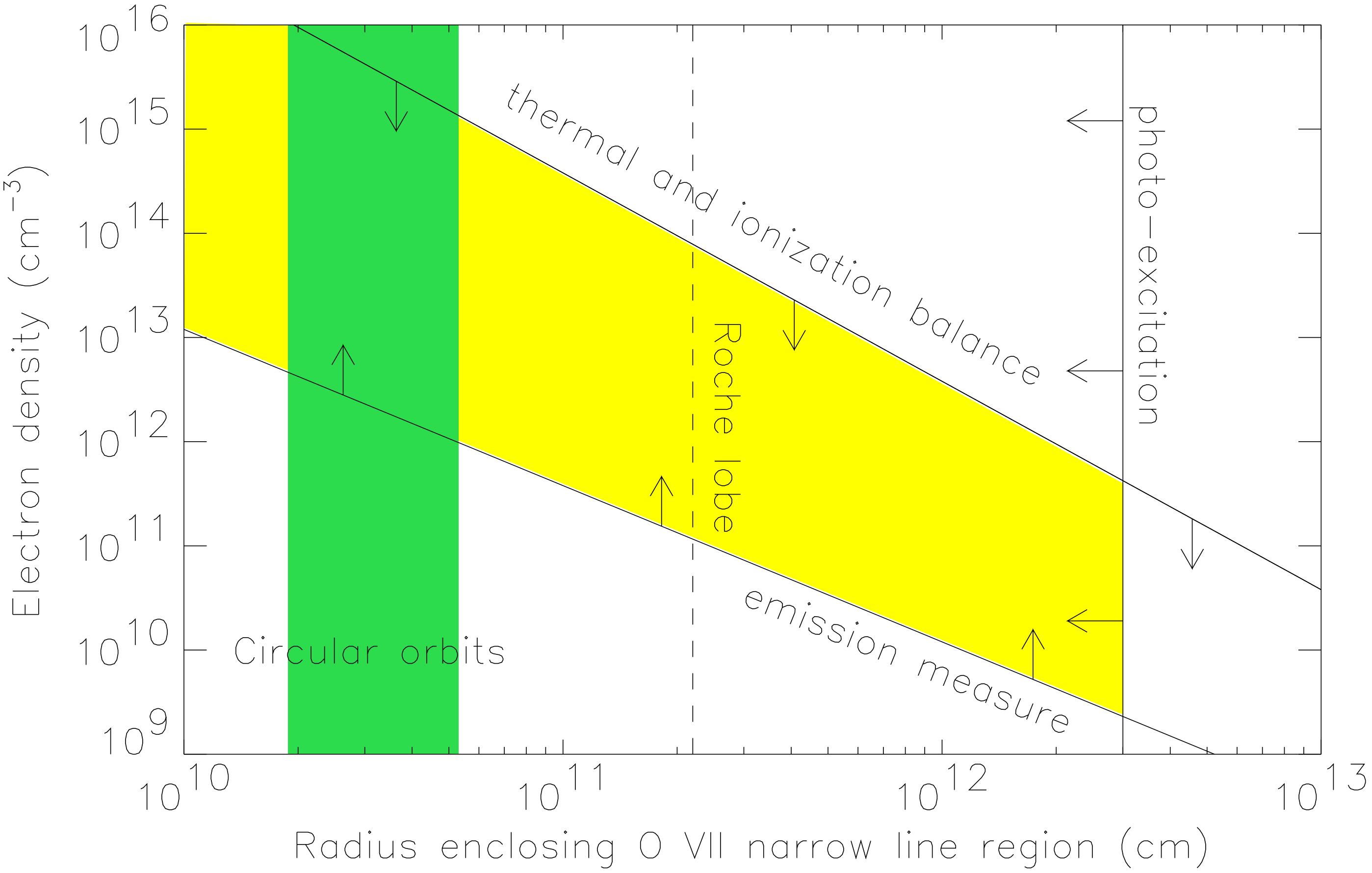

FIG. 7.— Confidence limits (90%) on the density and position of the narrow line emission region, obtained from spectroscopy and modeling. The limits shown correspond to O VII, and similar limits with N VI and Ne IX can be set.

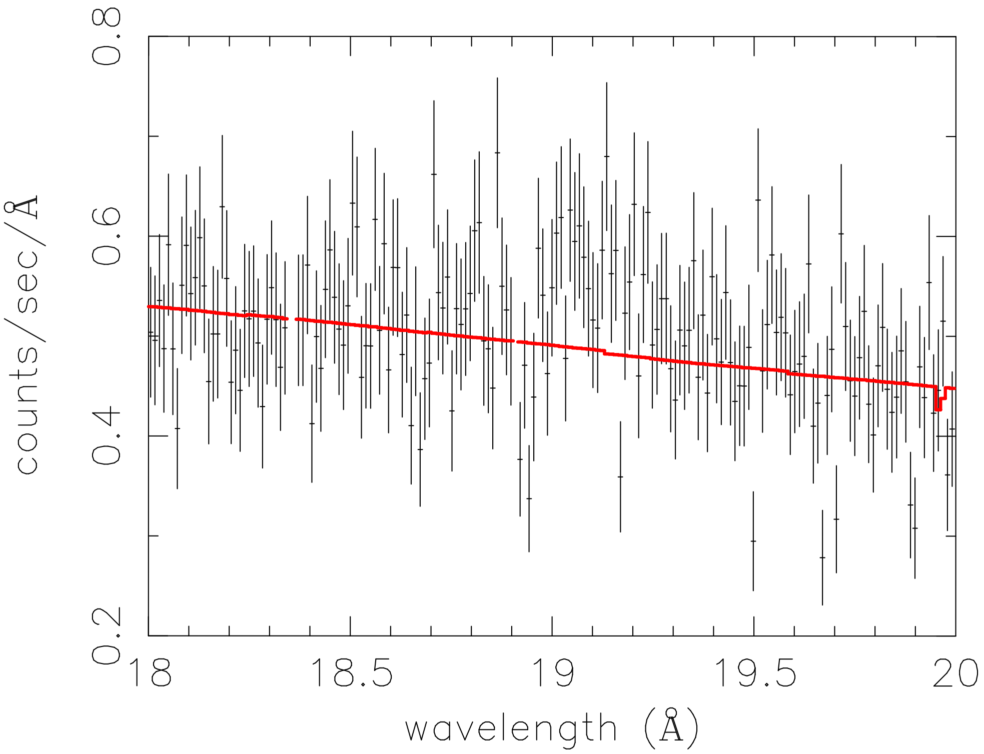

FIG. 8.— Main-on observation near the O VIII Lyα wavelength of 18.97 Å, at full resolution. Further observations are needed to determine whether there is a P Cygni feature.

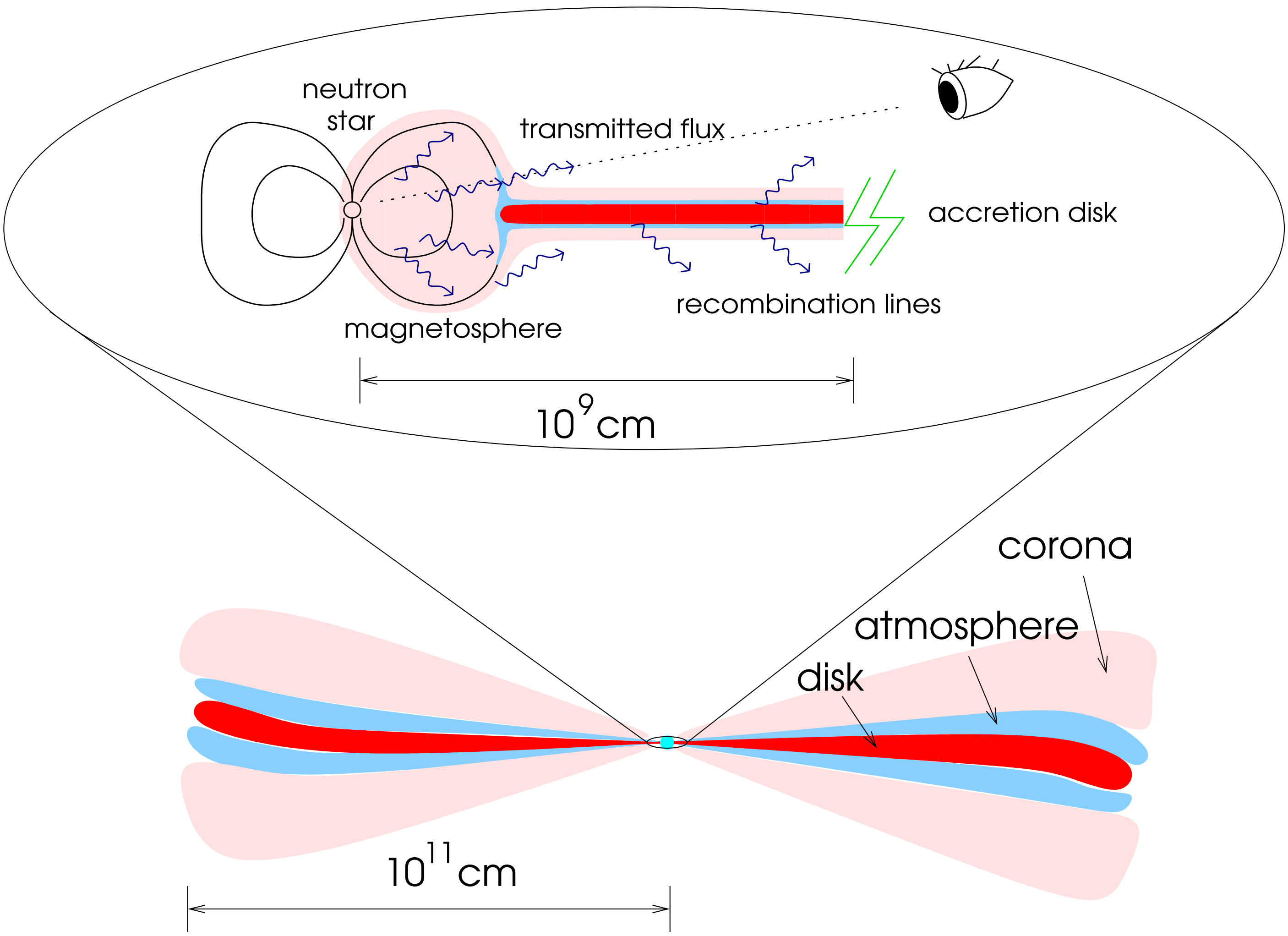

FIG. 9.— Hypothetical sketch of an accreting, magnetized neutron star, loosely based on the Ghosh & Lamb (1979) model. The accretion disk structure is also sketched, based on models by Jimenez-Garate, Raymond, Liedahl, & Hailey (2001). We define the atmosphere as a thin skin on the disk which is emitting X-ray recombination emission. The disk atmosphere and corona, or the illuminated face of the companion (not shown), may be responsible for the narrow line emission. Plasma from the inner disk can be channeled by the magnetic field, forming a highly ionized and possibly Compton-thick structure in the magnetosphere. This structure and the inner disk are potential sites for Compton scattering, X-ray absorption, and recombination emission. The tilt of the pulsar magnetic moment with respect to its spin axis is not shown.

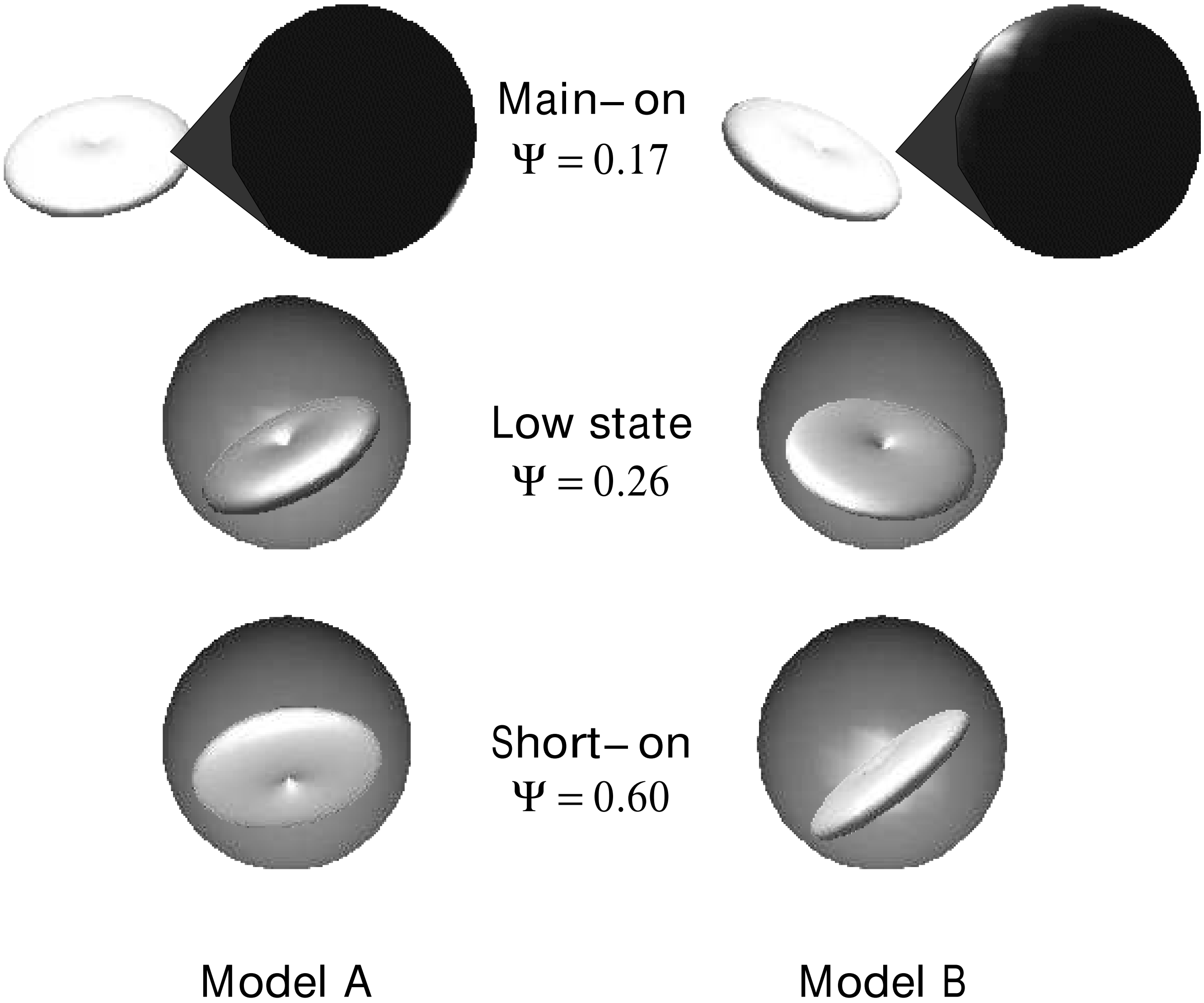

FIG. 10.— Schematic of the Her X-1 geometry during our three observations, showing the outer disk precession angle according to Model A (Gerend & Boynton 1976; Howarth & Wilson 1983), and to Model B (Scott, Leahy, & Wilson 2000). The diagram does not include disk warp, is roughly to scale, and is meant to show the projection of the system to our line of sight.

Table 1
Observations with the Reflection Grating Spectrometer

MJD[a] Interval	*XMM* Orbit	Observation Start	Exposure (ks)	Orbital Phase[(1)]	35 d Phase[b]	RGS 1 (c/s)[c]	RGS 2 (c/s)[c]
51935.036–51935.169	207	2001 Jan 26, 00:51:13 UT	11.31	0.18–0.26	0.17 (main-on)	11.29	···
51972.927–51973.083	226	2001 Mar 4, 22:14:18 UT	13.41	0.47–0.56	0.26 (low state)	0.37	0.42
51984.906–51985.053	232	2001 Mar 16, 21:45:01 UT	12.63	0.52–0.60	0.60 (short-on)	0.83	0.93

[a]Mean Julian Day.

[b]The zero of the 35 d phase is obtained at MJD 51929.08 ($\phi_{\rm orb}$ = 0.68) and MJD 51964.00 ($\phi_{\rm orb}$ = 0.22) from *RXTE ASM* dwell-by-dwell light curve data. The *ASM* light curve shows some evidence (a 4σ detection in one dwell) that the second turn-on occurred at MJD 51963.08 ($\phi_{\rm orb}$ = 0.68) instead, but is affected by pre-eclipse dips.

[c]First order count rates.

References. — (1) Deeter et al. 1998.

Table 2
Observed X-ray emission lines

Line(s)	λ_o (Å)	λ (Å)	σ (km/s)	Flux[a]	State	EW (eV)[b]	Counts [c]
C VI Lyα	33.74	33.72 ± 0.01	< 380	$6.4^{+2.1}_{-1.8}$	Low	2.7 ± 0.4	47
		33.75 ± 0.02	< 320	10^{+4}_{-3}	Short-on	1.8 ± 0.3	66
N VI Heα	29.53 (f)	···	···	< 0.94	Low	< 0.6	···
		···	···	< 1.6	Short-on	< 0.4	···
	29.08 (i)	29.07 ± 0.01	270 ± 100	29 ± 4	Low	18.6 ± 1.9[d]	173[d]
		29.10 ± 0.015	< 260	40 ± 6.5[e]	Short-on	10.9 ± 0.9[d]	217[d]
		···	···	$\lesssim 30$	Main-on	···	···
	28.78 (r)	28.77 ± 0.01	< 260	6.6 ± 2.0	Low	···	···
		28.75 ± 0.02	< 260	9 ± 5[e]	Short-on	···	···
N VII Lyα	24.78	$24.77^{+0.02}_{-0.01}$	< 590	15 ± 3	Low	5.2 ± 0.7	58
		24.80 ± 0.02	520^{+230}_{-180}	23 ± 5.5[e]	Short-on	4.8 ± 0.5	111
		24.85 ± 0.17	3200 (fixed)	84 ± 30	Main-on	···	···
O VII Heα	22.10 (f)	···	···	< 3.6	Low	< 2.8	···
		···	···	< 3.6	Short-on	···	···
	21.80 (i)	21.79 ± 0.01	< 400	31 ± 5	Low	23.4 ± 2.4[d]	154[d]
		21.82 ± 0.02	320^{+140}_{-160}	70 ± 10	Short-on	22.4 ± 1.6[d]	287[d]
		···	3200 ± 800	155 ± 30	Main-on	···	···
	21.60 (r)	21.61 ± 0.03	< 1600	10 ± 4	Low	···	···
		21.62 ± 0.02	···	8 ± 4	Short-on	···	···
		···	3200 ± 800	38 ± 8	Main-on	···	···
O VIII Lyα	18.97	18.96 ± 0.01	390 ± 200	12.0 ± 2.5	Low	7.5 ± 0.8	98
		$18.96^{+0.02}_{-0.01}$	< 450	14 ± 3	Short-on	3.0 ± 0.3	85
		19.05 ± 0.05	P Cygni?	$\lesssim 90$	Main-on	···	···
Ne IX Heα	13.70 (f)	···	···	$\lesssim 1.6$	Low	···	···
		···	···	< 6.2	Short-on	···	···
	13.55 (i)	···	···	$5.6^{+2.5}_{-2.1}$	Low	10.1 ± 1.7[d]	44[d]
		···	···	12^{+3}_{-4}	Short-on	7.2 ± 1.0[d]	61[d]
	13.45 (r)	···	···	< 4.8	Low	···	···
		···	···	$3.9^{+3.1}_{-2.2}$	Short-on	···	···
Ne X Lyα	12.13	12.20 ± 0.04	···	7 ± 3	Low	···	···
		···	···	3.6 ± 3.0	Short-on	···	···

Note. — Errors are 90 % confidence limits unless otherwise noted. Symbols: λ_o = theoretical wavelength; λ = measured wavelength; σ = standard deviation; State = Flux state within the Her X-1 35 d cycle; *EW* = equivalent width. Note λ, σ and the flux are obtained from Gaussian fits.

[a]In units of 10^{-5} phot cm^{-2}s^{-1}. The errors do not include the continuum level uncertainty, which can be significant for the weakest lines.

[b]Quoted errors in this column are 1-σ (68 % confidence limits).

[c]After pipeline processing and application of response matrices, these are the corrected X-ray counts per line (or line complex) with the local continuum subtracted. The *EW* is then calculated.

[d]These measurements include both intercombination (i) and resonance (r) lines.

[e]We use only RGS 2 data in these line fits, to avoid a few flagged pixels in RGS 1. The RGS 1 still detects these lines at levels comparable to RGS 2.

TABLE 3
CONTINUUM POWER-LAW FIT PARAMETERS

State	Photon Index	Normalization at 1 keV (phot $\mathrm{keV^{-1}\ cm^{-2}\ s^{-1}}$)	N_H (10^{18} $\mathrm{cm^2}$)	χ^2/DOF
Low	1.65 ± 0.06	$(4.1 \pm 0.1) \times 10^{-3}$	< 86	$562/467^{a} = 1.21$
Short-on	1.75 ± 0.03	$(9.8 \pm 0.2) \times 10^{-3}$	< 75	$1179/945^{a} = 1.25$
Main-on	1.88 ± 0.10	0.130 ± 0.007	< 57	$4312/3122 = 1.39$

Note. — Errors are 90% confidence limits. DOF = degrees of freedom.
[a]The DOF reflect rebinning performed for plotting and fitting the continuum.

TABLE 4
HELIUM-LIKE LINE DIAGNOSTICS AND PHOTOEXCITATION OF THE 2^3S LEVEL

Ion	Her X-1 State	$R = f/i$ Line Ratio	$G = (f+i)/r$ Line Ratio	$\lambda_{\mathrm{f}\to\mathrm{i}}$ (Å)[1]	Flux $F_{\lambda_{\mathrm{f}\to\mathrm{i}}}$ (10^{-13} erg $\mathrm{cm^{-2}\ s^{-1}\ Å^{-1}}$)	w_{f} $2^3S \to 1^1S$ Rate (s^{-1})[2]	$w_{\mathrm{f}\to\mathrm{i}}(r{=}10^{11}\mathrm{cm})$ $2^3S \to 2^3P$ Rate (s^{-1})	d_{crit} Radius (cm)
Ne IX	low	< 0.3	> 1.3	1270	1.9 ± 0.1[3]	1.09×10^4	5×10^5	7×10^{11}
	short-on	< 0.5	$3.8^{+16}_{-2.1}$					
O VII	low	< 0.14	3.1 ± 1.4	1637	1.5 ± 0.2[3]	1.04×10^3	1×10^6	3×10^{12}
	short-on	< 0.06	8.7 ± 4.5					
N VI	low	< 0.04	4.4 ± 1.5	1906	1.5 ± 0.1[4]	2.53×10^2	2×10^6	9×10^{12}
	short-on	< 0.05	4.4 ± 2.6					

Note. — Errors are 90% confidence limits. Symbols: $\lambda_{\mathrm{f}\to\mathrm{i}}$ = wavelengths of $2^3S \to 2^3P$ transitions; $w_{\mathrm{f}\to\mathrm{i}}$ = radiative decay rates; $w_{\mathrm{f}\to\mathrm{i}}$ = calculated photoexcitation rate.

References. — (1) Porquet et al. 2001; (2) Drake 1971; (3) from the *Hubble GHRS* at $\phi = 0.56$–0.60 by Boroson et al. 1996; (4) from the *Hubble FOS* at $\phi \sim 0.5$ by Anderson et al. 1994.

TABLE 5
ABSORPTION FEATURES

Edge	λ_{o} (Å)	λ (Å)	τ	State
Neutral O	23.05	23.0 ± 0.5	0.30 ± 0.06	Low
	23.05	$23.27^{+0.10}_{-0.13}$	0.28 ± 0.04	Short-on
	23.05	$23.1^{+0.1}_{-0.2}$	0.22 ± 0.02	Main-on
Neutral N	30.77	(fixed)	< 0.08	Main-on
Line	**λ_{o} (Å)**	**λ (Å)**	**EW (eV)**	**State**
Atomic O 1s-2p	23.47[1]	$23.50^{+0.03}_{-0.02}$	0.57 ± 0.30	Main-on

Note. — Errors are 90% confidence limits. Symbols: λ_{o} = theoretical edge wavelength; λ = measured wavelength; τ = edge optical depth; EW = equivalent width.

References. — (1) McLaughlin & Kirby 1998.

Table 6
Elemental abundance measurements and differential emission measure (DEM) parameters

State	$\frac{(C/O)}{(C/O)_\odot}$	$\frac{(N/O)}{(N/O)_\odot}$	$\frac{(Ne/O)}{(Ne/O)_\odot}$	K (10^{58} cm^{-3})	γ	χ^2 of Fit (1 DOF)	Ionizing Spectrum
Low	0.52 ± 0.12	8.8 ± 1.0	1.9 ± 0.7	7.2 ± 3.7	1.59 ± 0.17	0.02	P.L.+cut (main-on)
Short-on	0.56 ± 0.15	7.7 ± 0.9	2.5 ± 0.7	33^{+17}_{-11}	2.05 ± 0.19	4.96	P.L.+cut (main-on)
Low	0.30 ± 0.07	5.9 ± 0.7	2.5 ± 1.0	10^{+4}_{-3}	1.78 ± 0.17	1.25	20 keV brems.
Short-on	0.29 ± 0.08	4.6 ± 0.6	3.5 ± 1.0	43^{+17}_{-13}	2.28 ± 0.19	8.72	20 keV brems.

Note. — We show the statistical errors at 66% confidence. The element abundance ratios (by number of atoms) are normalized to the solar values compiled by Wilms, Allen, & McCray (2000), which are $(C/O)_\odot = 0.47$, $(N/O)_\odot = 0.11$, and $(Ne/O)_\odot = 0.14$. The K and γ parameters define the DEM.